Delft University of Technology

Energy & Process Technology - Mechanical Engineering
MSc Thesis

# Thermally driven metal hydride cooling systems for fishing vessels

*Author:*

Lars Steverink (4328140)

*Thesis committee:*

Dr. ir. C.A. Infante Ferreira, supervisor

Ir. C. Hellinga, supervisor

Prof. dr. ir. T.J.H. Vlugt

Dr. ir. M. van der Pal

June 30, 2021

# Acknowledgements

While writing this thesis I have received a tremendous amount of support and well placed assistance.

First, I would like to thank my supervisors Carlos and Chris, whose expertise, insights and feedback were invaluable to bringing my work to a higher level and keeping on track with my progress.

Second, I would like to thank my girlfriend, Bauke, for supporting me, helping me and listening to my explanations, while you are truly a liberal arts fanatic.

Third, I would like to thank my family. You have always tried to help me wherever you could. A special thanks for Lisa, my big sister, for proofreading my thesis.

Last, I would like to thank my friends, who have always distracted me in a positive manner and did not make me forget that there are other things in life.

**Abstract**

On the island of Goeree-Overflakkee, local and regional municipalities, businesses and education and knowledge institutions are pursuing a pioneering project called H2GO. The H2GO project is a project that researches the role green hydrogen can fulfill in our society through eight different scalable sub-projects. One of these projects is making the local fishing fleet of Goeree-Overflakkee $CO_2$ neutral. Due to technical limitations, adaptations to make the fishing vessels $CO_2$ neutral will not be possible for the coming years. For the shorter term, the project is therefore also looking for different ways to make the fleet more sustainable. A substantial polluting factor for this type of fishing vessels is the refrigeration unit, used to cool the freshly caught fish. A technology, called thermally driven metal hydride cooling, shows potential to provide an alternative for the current refrigeration system. In this thesis, the technical feasibility is explored of replacing the conventional ice slurry machines that fishing vessels currently employ with this technology. In order to do this, a literature review on different types of metal hydrides and the state-of-the-art on metal hydride cooling systems has been conducted. After this, a numerical model is presented and validated with an equivalent model and experiments. The model shows good similarity regarding overall system performance compared to the experiments. Finally, a metal hydride cooling system, containing another low temperature metal hydride is proposed that is capable of achieving a cooling capacity of 16 kW at a cooling temperature of -10 to -20 °C. This leads to the conclusion that the system has some efficiency drawbacks, but that the metal hydride system is technically feasible for use in the fishing vessels at Goeree-Overflakkee. This, in return, reveals a significant opportunity for employing this new technology to lower the environmental impact of the Goeree-Overflakkee fishing fleet.

# Contents

# List of Abbreviations

| | | |
|---|---|---|
| **COP** | Coefficient of performance | |
| **DAE** | Differential and algebraic equations | |
| **FC** | Fuel cell | |
| **HTF** | Heat transfer fluid | |
| **MHCS** | Metal hydride cooling system | |
| **MHHP** | Metal hydride heat pump | |
| **MH** | Metal hydride | |
| **PCT** | Pressure-Concentration-Temperature | |
| **PMHT** | Purdue Metal Hydride Toolbox | |
| **SCP** | Specific cooling power | $\frac{W}{kg}$ |
| **SL** | Standard litre | |

# Nomenclature

| | | |
|---|---|---|
| $\alpha$ | Heat transfer coefficient | $W/m^2K$ |
| $\Delta$H | Enthalpy of formation | $J/mol\ H_2$ |
| $\Delta$S | Entropy of formation | $J/mol\ H_2\ K$ |
| $\Delta$T | Temperature difference | $K$ |
| $\epsilon$ | Heat exchanger effectiveness | |
| $\zeta$ | Porosity | |
| $\lambda$ | Thermal conductivity | $W/mK$ |
| $\rho$ | Density | $kg/m^3$ |
| $\Omega$ | Area of hydrogen connection tube | $m^2$ |

| | | |
|---|---|---|
| $A$ | Surface area | $m^2$ |
| $C_p$ | Specific heat capacity | $J/kgK$ |
| $De$ | External diameter heat transfer fluid tube | $m$ |
| $E$ | Activation energy | $J/mol$ |
| $f_s$ | Slope factor | |
| $h$ | Convection heat transfer coefficient | $W/m^2K$ |
| $K$ | Reaction rate constant | |
| $L$ | Length heat transfer fluid tube | $m$ |
| $MH_2$ | Molar mass of hydrogen | $kg/mol$ |
| $m$ | Mass | $kg$ |
| $\dot{m}$ | Mass flow | $kg/s$ |
| $n_{tubes}$ | Number of heat transfer fluid tubes | |
| $NTU$ | Number of transfer units | |
| $P$ | Pressure | bar |
| $\dot{Q}$ | Heat flow | $W$ |
| $R$ | Universal gas constant | $8.314\ J/K\ mol$ |
| $S$ | Distance between heat transfer tubes | $m$ |
| $T$ | Temperature | $^\circ C$ |
| $t$ | Time | $s$ |
| $U$ | Overall heat transfer coefficient | $W/m^2K$ |
| $V$ | Reactor volume | $m^3$ |
| $\vec{u}$ | Velocity | $m/s$ |
| $w$ | Hydrogen concentration | $\frac{weight\ H_2}{weight\ \mathrm{MH}}\ \%$ |
| $X$ | Concentration | $mol/mol$ |

| | |
|---|---|
| $x$ | Transition period coefficient |

## Subscripts

| | |
|---|---|
| $\alpha$ | $\alpha$-region |
| $\beta$ | $\beta$-region |
| $A$ | Reactor A |
| $abs$ | Absorption |
| $B$ | Reactor B |
| $c$ | Cooling |
| $des$ | Desorption |
| $eff$ | Effective |
| $eq$ | Equilibrium |
| $g$ | Gas |
| $h$ | Hot |
| $H_2$ | Hydrogen gas |
| $HTF$ | Heat transfer fluid |
| $i$ | In |
| $k$ | Critical |
| $m$ | Ambient |
| $MH$ | Metal hydride |
| $mid$ | Middle |
| $mm$ | Metallic mass |
| $o$ | Out |
| $s$ | Solid |
| $trans$ | Transition |

| | |
|---|---|
| $w$ | Water |

# 1 Introduction

With climate change becoming an increasingly pressing ecological and economic issue, the urgency to increase the worldwide implementation of sustainable energy technologies across various industries is continuously growing. One industry where this urgency is especially apparent is the refrigeration industry. Due to economic growth in countries around the world, the demand for refrigeration has been rapidly increasing, especially in tropical countries. It is estimated that 27% of the household energy consumption comes from cooling and refrigeration [1]. Because conventional refrigeration fluids are known to be hazardous to the environment, it is of vital importance that this need is met with more sustainable alternatives. More sustainable options, such as lithium bromide - water absorption systems are already implemented in different areas. These absorption systems can use waste heat to generate a cooling effect. The Coefficient of Performance (COP) of lithium bromide - water absorption systems is generally in the range of 0.6 to 0.8 for single effect systems [2]. Unfortunately, however, Lithium Bromide - water absorption systems are limited in their operating range and are therefore not suitable for freezing applications. Other options, such as green hydrogen gas must for that reason be investigated.

One of the projects that investigates the option of using green hydrogen is a project called H2GO. The H2GO project is a pioneering project by Delft University of Technology, regional and local municipalities, residents and local and international businesses on the island of Goeree-Overflakkee, South-Holland, the Netherlands. The island of Goeree-Overflakkee is an island that already produces green energy from the wind and the sun on a large scale. H2GO explores the potential and feasibility to use this green energy to create a green hydrogen economy on the island. In order to create this economy, it dives into the question how green hydrogen gas can be applied to live, travel work and recreate on the island more sustainably.

H2GO is divided into eight different sub-projects. One of these sub-projects focuses on making the large fishing fleet that is present on the island more sustainable. The final goal of this sub-project is to sail without $CO_2$ emissions. Since batteries are heavy, hydrogen is deemed a more interesting option to lower the emissions of these ships. However, at this moment sailing on open sea for multiple days purely on hydrogen is technically very difficult, due to limited storage space for the hydrogen. Because of this, the flyshooter fishing fleet will be sailing on diesel for the coming years. Fortunately, there are other options to lower the emissions of the fleet than the fuel usage. The refrigeration units present on these type of flyshooter ships, for example, currently constitute a sizable polluting factor. An average flyshooter has a 16 kW-ice slurry refrigerator on board to keep the caught fish fresh for some days. By replacing this with a hydrogen-based refrigerator the greenhouse gasses emitted by the fleet may be reduced. Hydrogen can be produced in a neutral $CO_2$ emission way and can therefore fulfil an interesting role in this application.

Over the past couple of decades, a significant amount of research on the utilization of hydrogen as a working fluid for power generation and thermal management has been performed. One of the obstacles these studies have revealed is that hydrogen occupies a relatively large volume per unit mass and is highly flammable, which makes storage and transport are a significant concern in the implementation of hydrogen in this sector.

Fortunately, metal hydride (MH) alloys offer a solution to the issue of storage, because they can store a large

volume of hydrogen per unit mass as a solid solution which is why it could be a high-quality hydrogen storage medium. A unique characteristic of metal hydrides is that they can be altered to be implemented in a wide range of temperatures (-40 [U+25E6]C to 800 [U+25E6]C) [3]. Metal hydride systems can be used for storage, hydrogen purification, hydrogen compression and thermally driven machines, such as cooling, heating, thermal storage and hydrogen compressors. Because of its potential, research in the use of metal hydrides in cooling systems gained importance. In some areas, it has even found practical applications, though in other areas it is unclear whether it is possible to use. This study will explore the knowledge that has been acquired over the past few decades about the application of metal hydrides in cooling systems. It will first provide background information about MH alloys, then expand upon literature about its use in cooling systems. After this, this thesis will present a numerical model implemented in SIMULINK. This SIMULINK model is used to explore the possibilities of replacing the 16 kW refrigeration unit generating ice slurry with a sustainable metal hydride cooling system. The model will be validated by comparing the simulation results with an equivalent model and the experiments used to validate that model. Lastly, a new metal hydride will be introduced into the system to investigate the feasibility of a metal hydride cooling ice slurry system.

## 1.1 Research questions

The goal of this thesis project is to investigate whether the H2GO project could replace the flyshooter ice slurry refrigerators with a more sustainable metal hydride cooling system. This cooling system needs to generate a cooling effect at -10 to -20 °C, with a cooling capacity of 16 kW.
The main research question of this thesis is the following:

- How technically feasible is it to generate a cooling effect of 16 kW at -10 to -20 °C on a diesel powered fishing vessel with a metal hydride cooling system?

The sub questions to answer the research question are:

- How does a thermally driven metal hydride cooling system work and what are its limitations?
- How are numerical models, simulating metal hydride cooling systems, developed?
- How does a MHCS perform under different operating conditions and how does the reaction rate constant K influence the performance?

First, a literature review will be performed to provide an overview of the state-of-the-art on metal hydride cooling systems. Second, a numerical model will be created to simulate a metal hydride cooling system in detail. The literature review and numerical model will then be used to explore the limitations of the system and investigate the different influences on performance. Finally, a conclusion will be drawn, whether metal hydride cooling systems can be used to generate ice slurry on fishing vessels.

# 2 Metal hydride background information

## 2.1 Formation of metal hydride and working principle

Metal hydrides are formed by a reversible chemical reaction when hydrogen is absorbed in a metal at a certain temperature and pressure, called the absorption process. The absorption process is an exothermic process generating large amounts of heat. When heat is applied to a metal hydride this process is reversed through an endothermic reaction, called the desorption process [4]. Metal hydride cooling systems have the same working principle as conventional sorption systems, e.g. silica gel/water, $LiBr/H_2O$. The major difference is that a metal hydride/hydrogen cooling system uses a non-condensable working fluid.

At least two reactors, using different metal hydrides, are needed. The reactors replace the condenser/evaporator and generator/absorber present in conventional sorption systems [5]. The absorption process occurs through the following reactions:

$$\mathrm{M} + \tfrac{\mathrm{x}}{2}\,\mathrm{H_2} \longrightarrow \mathrm{MH}_x + \mathrm{Heat}\,(\alpha\text{-phase})$$
$$\mathrm{MH}_x + \tfrac{\mathrm{y\text{-}x}}{2}\mathrm{H_2} \longrightarrow \mathrm{MH}_y + \mathrm{Heat}\,(\beta\text{-phase})$$

Desorption will occur in the opposite direction.

The $\alpha$-phase is a solid solution phase in which the initial hydrogen molecules dissociate into atoms and diffuse into the metal. A sharp increase in pressure at a constant temperature can be measured during the $\alpha$-phase. Upon reaching final concentration, when all metal atoms have formed chemical bonds with hydrogen atoms, the $\beta$ phase completes the formation of the metal hydride. If more hydrogen is added a further increase in pressure will be measured as hydrogen will be present in gaseous state. An intermediate region named $\alpha+\beta$-phase exists between the two phases. A gradual conversion of $\alpha$ to $\beta$ will occur in this phase, ideally increasing concentration at a constant temperature and equilibrium pressure ($P_{eq}$) [3].
The absorption of hydrogen, at the $\alpha+\beta$-phase, into an alloy is composed by five steps [6]:

1. physisorption of hydrogen molecules
2. dissociation of hydrogen molecules and chemisorption
3. surface penetration of hydrogen atoms
4. diffusion of hydrogen atoms through the alloy, by interstitial or vacancy mechanisms
5. the formation of metal hydrides

Desorption will occur in the opposite direction. Figure 1 presents a Pressure-Concentration isotherm diagram and a Van't Hoff plot, together called a Pressure-Concentration-Temperature (PCT) diagram. The PCT characteristics link the metal hydride equilibrium pressure to the hydrogen concentration and metal hydride temperature.

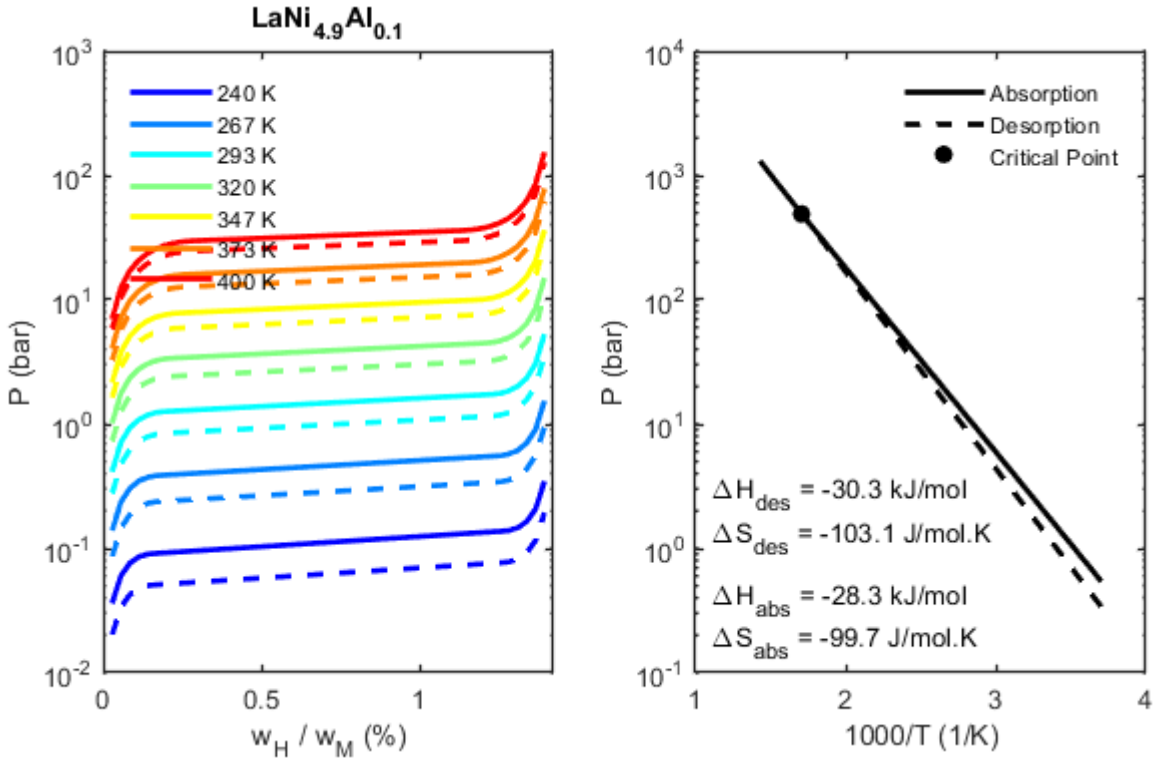


Figure 1: Non-ideal Pressure-Concentration-Temperature diagram of $LaNi_{4.9}Al_{0.1}$ extracted from the Purdue Metal Hydride Toolbox [9]. Note that the temperature is measured in inverse Kelvin ($K^{-1}$)

.

As can be seen in figure 1 there is a sloped plateau and hysteresis effect in the $\alpha + \beta$-phase during absorption and desorption. Hysteresis is an asymmetry in pressure ratio during absorption and desorption, caused by deformations and material stresses. Hysteresis affects the performance of metal hydride systems significantly in a negative way, as it represents an irreversible pressure loss. The sloped plateau also indicates a reduction in efficiency of a metal hydride absorption and desorption cycle and is defined by the expression [7]:

$$f_s = \frac{d\, ln(P_{eq})}{d\, w} \tag{1}$$

Due to the plateau slope, the equilibrium pressure will increase in the $\alpha + \beta$-phase during absorption and will decrease in the $\alpha + \beta$-phase during desorption, and therefore decreases the usable hydrogen capacity and system performance [8]. All metal hydride systems will have sloped plateaus and exhibit hysteresis, except at critical temperature $T_k$. The amount of hysteresis asymmetry and size of the sloped plateau region varies between alloys.

Other important properties are enthalpy of formation ($\Delta H$), equilibrium pressure ($P_{eq}$), metal hydride temperature ($T$), entropy of formation ($\Delta S$) and hydrogen concentration ($w$). The Modified van't Hoff equation estimates the equilibrium pressure (in Pa) to the other properties by the following equation [7, 10, 11]:

$$lnP_{eq} = -\frac{\Delta H}{RT} + \frac{\Delta S}{R} + f_s(w - w_{mid}) \tag{2}$$

Where R is the universal gas constant.

## 2.2 Classification of metal hydrides

The term 'metal hydride' refers to the metal hydride phase of the absorption hydrogen in metal, but in general it is simplified to any alloy capable of reacting with hydrogen to form a metal hydride phase [7].

Classification of metal hydrides can be done on the basis of the bonds between alloy and hydrogen atoms. These bonds can be ionic, covalent and metallic. Ionic bonds, with the exception of magnesium hydrides, are too stable to be used in engineering applications. Covalent bond hydrides can only be formed under special conditions, not suitable for practical systems. Only metallic bonds offer the characteristics needed for storing hydrogen with fast reaction kinetics. Metallic bonds and their corresponding metal hydrides are classified with respect to the amount of alloy atoms in one mole of metal hydride. Low electro-negative metals, called A-metals, form stable hydrides with too high desorption temperatures or too low equilibrium pressures. A-metals have strong hydriding properties and are the main contributor to hydrogen absorption. Examples of A-metals are: Na, K, Li, La and Ti. B-metals are more electro-negative than A-metals and do not form hydrides at relevant pressures and temperatures. B-metals have weak hydriding properties, but their presence is necessary as it increases the hydriding kinetics of the metal hydride alloy. Throughout the years metal hydride alloys, containing A- and B-metals, have been produced to increase the metal hydride phase stability at relevant pressures and temperatures for heat pumps and cooling systems. There are four A-B-metal hydride alloy structures: $A_2B$, AB, $AB_2$ and $AB_5$ [8]. Temperature and pressure conditions of the absorbing and desorbing reactions depend on the application, but in general are between $T \approx 240 - 750$ K and $P \approx 1 - 100$ bar [7]. In table 1, an overview of different metal hydride structures is shown.

Table 1: Overview of A-B-metal hydride classification structures [7]

| Structure | Example |
|---|---|
| $A_2B$ | $Zr_2Cu$, $Ti_2Pd$, $Mg_2Ni$ |
| AB | LaNi, MgNi, TiFe, ZrCo |
| $AB_2$ | $TiMn_2$, $CaNi_2$, $GdCo_2$, $ZrMn_2$, $ZrCr_2$, $TiCr_2$, $Ti0.99Zr_{0.01}V_{0.43}Fe_{0.09}Cr_{0.05}Mn_{1.5}$ |
| $AB_5$ | $LaNi_5$, $YCo_5$, $EuNi_5$, $CaNi_5$, $LaCo_5$, $LaNi_{4.9}Al_{0.1}$, $LmNi_{4.91}Sn_{0.15}$ |

## 2.3 Metal hydride alloy selection

Metal hydride cooling systems have been designed with a variety of different configurations and capabilities. Experimental and computational studies are mainly focused on heat and mass transfer characteristics instead of metal hydride selection. Yang et al. [12] proposed a selection method for metal hydrides in metal hydride heating and cooling systems. First, the hysteresis and plateau slopes of the metal hydrides are taken into consideration and the metal hydrides need to fit the operating conditions. Second, the performance of the alloys are compared to others to select better pairs.

Voskuilen et al. [9] developed a method and database to conduct the material selection for thermal metal hydride systems. They have presented the method and database as a MATLAB script, called the Purdue Metal

Hydride Toolbox (PMHT). The PMHT includes metal hydride property data from the Sandia hydride database [13] and more recent data from literature (up till 30 May 2014). Every hydride present in the toolbox contains, at least, the hydride type, composition, hydrogen capacity and desorption thermodynamics. See figure 1 for an example of an PCT diagram extracted from this database.

## 2.4 Metal hydride alloy selection

The PCT characteristics and, for example, enthalpy of formation of metal hydride alloys determine its possible applications. Because of this not all alloys are suited for the use in a refrigeration system. In this subsection a preliminary selection of metal hydride alloys will be given that can generate useful cold between -20 - 0 °C. The PMHT will be used for a selection of high and low temperature alloys. The selection has been made by analyzing the PCT diagrams of the corresponding alloys.

### 2.4.1 Low temperature metal hydride alloy

The low temperature MH alloy to be used in the production of ice slurry needs to be able to generate useful cold between -20 - 0 °C. The alloy needs to be able to absorb hydrogen and generate heat $Q_m$ at a $T_m$ of 3 - 22 °C [14]. Also, the equilibrium pressure of the alloy needs to be between 1 - 150 bar at -20 °C $\leq T \leq$ 20 °C. To have reasonable performance the alloy should have small hysteresis and plateau slope and a high enthalpy of formation, but for this first selection only the PCT characteristics will be taken into consideration.

The PMHT database was used to examine 337 MH alloys for their usability at the conditions mentioned above. 74 MH alloys fit the PCT characteristic demands, mentioned above. As can be seen in figure 2, the alloy $La_{0.4}Pr_{0.6}Co_5$ has an equilibrium pressure between 1 - 150 bar at $T_c$ and $T_m$. See table 2 for an overview of the low temperature MH alloys and their characteristics.

### 2.4.2 High temperature metal hydride alloys

The high temperature alloy needs to be able to operate at 3 °C $\leq T_m \leq$ 22 °C and 80 °C $\leq T_h \leq$ 500 °C [14, 15, 16]. Driving temperature $T_h$ will come from either exhaust gases or coolant from the diesel engine present in the ship.

The PMHT database showed that 20 MH alloys fit the PCT characteristic demands for the high temperature alloy. Every single high temperature metal hydride alloy that has been selected may also be used as a low temperature alloy, but in general they exhibit less favorable characteristics, such as a larger hysteresis and slope at low temperatures compared to alloys that are purely selected as a low temperature alloy. Figure 3 shows the PCT diagram of $Ti_{0.8}Zr_{0.2}Mn_{1.5}Fe_{0.5}$. The equilibrium pressures from -10 to 80 °C are between 1 - 100 bar and therefore this alloy may be used as both a low and high temperature alloy. See table 3 for an overview of the high temperature MH alloys and their characteristics.

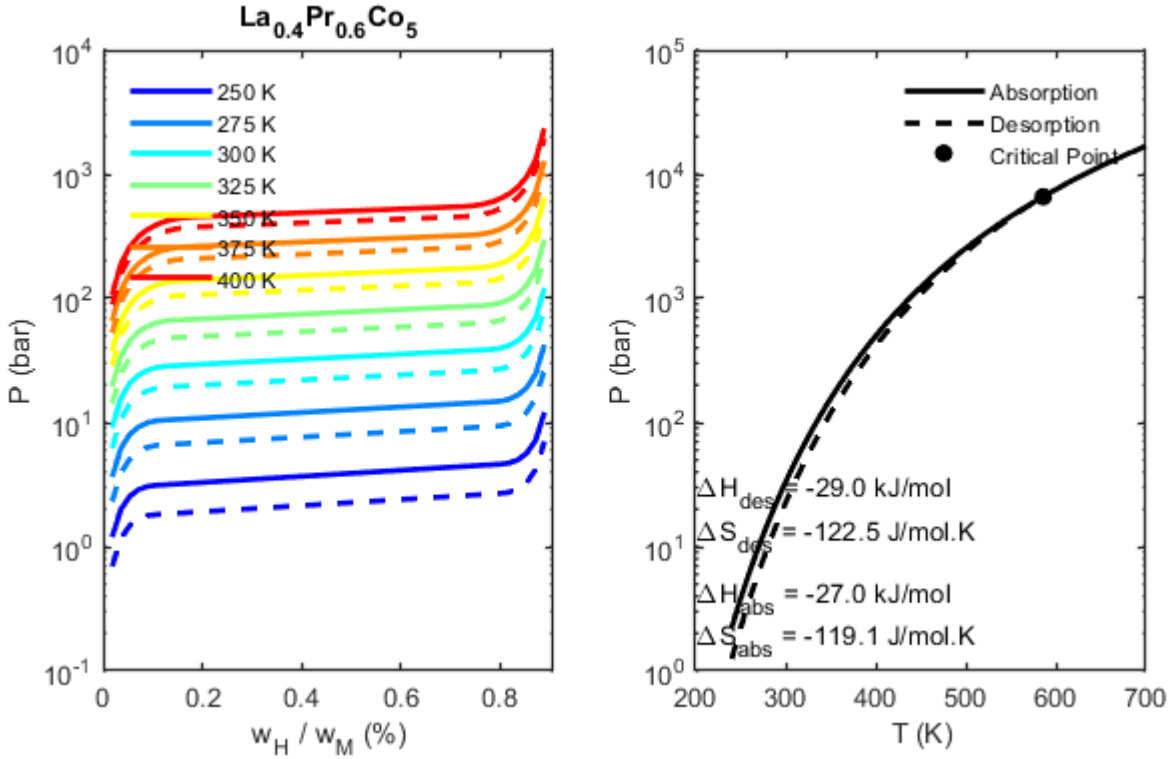


Figure 2: Non-ideal Pressure-Concentration Isotherm and van 't Hoff plot of $La_{0.4}Pr_{0.6}Co_5$ extracted from the Purdue Metal Hydride Toolbox [9]. Note that the temperature is measured in Kelvin (K).

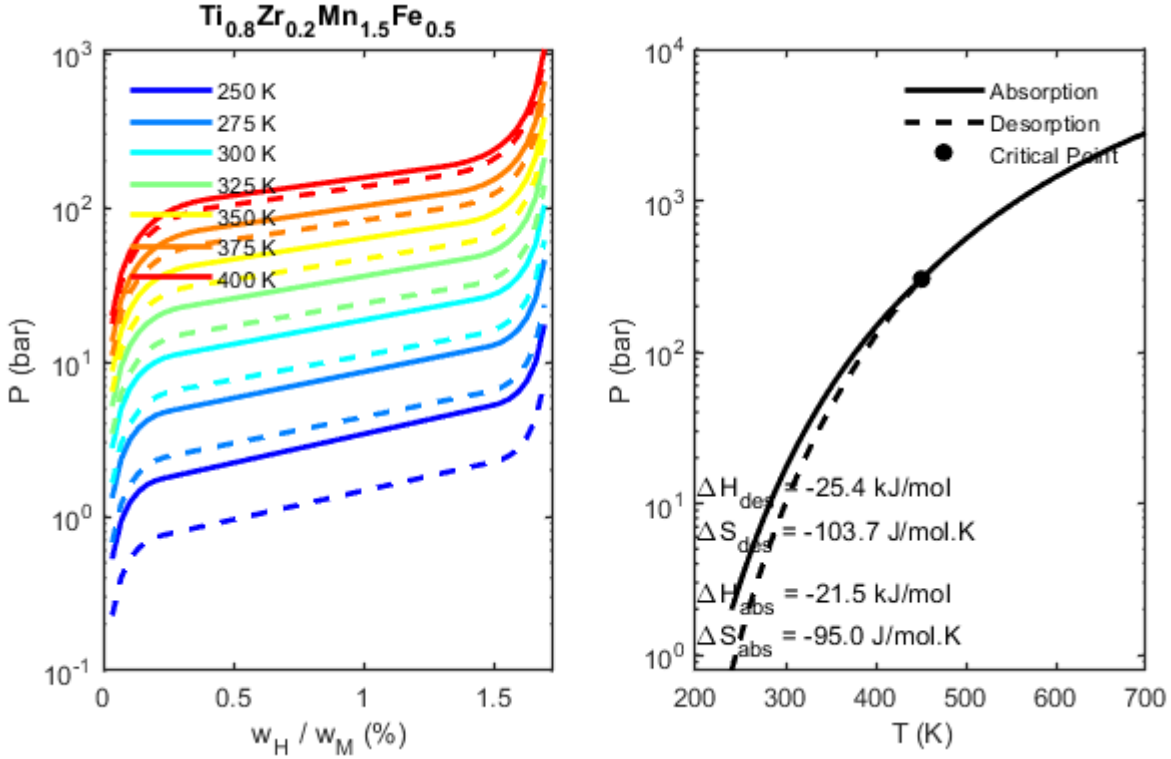


Figure 3: Non-ideal Pressure-Concentration Isotherm and van 't Hoff plot of $Ti_{0.8}Zr_{0.2}Mn_{1.5}Fe_{0.5}$ extracted from the Purdue Metal Hydride Toolbox [9]. Note that the temperature is measured in Kelvin (K).

Table 2: Low temperature metal hydride selection, extracted from the Purdue Metal Hydride Toolbox [9].

| Name | Type | Absorption | | Desorption | | M | $\rho$ | $C_p$ | $T_k$ | w |
|---|---|---|---|---|---|---|---|---|---|---|
| | | $\Delta H(J/molH_2)$ | $\Delta S(J/molH_2K)$ | $\Delta H(J/molH_2)$ | $\Delta S(J/molH_2K)$ | $(kg/kmol)$ | $kg/m^3$ | $J/kgK$ | $(K)$ | (%) |
| Ce0.5La0.5Ni2.5Cu2.5 | AB5 | -20934* | -83.64* | -22900 | -87 | 445.11 | 8200 | 419 | 586 | 1.13 |
| Ce0.7La0.7Ni5 | AB5 | -23034* | -101.86* | -25000 | -105.22 | 488.78 | 8200 | 419 | 586 | 1.4 |
| Ce0.8La0.2Ni4.7Cu0.3 | AB5 | -22880 | -111 | -30053 | -127.4 | 434.80 | 8200 | 419 | 437.4 | 1.60 |
| Ce0.8La0.2Ni5 | AB5 | -19192 | -103.2 | -24640 | -111.8 | 433.30 | 8200 | 419 | 633.5 | 1.38 |
| CeNi4.5Al0.5 | AB5 | -23650 | -105.1 | -27044 | -110.1 | 417.70 | 8200 | 419 | 678.8 | 1.43 |
| CeNi4.5Mn0.5 | AB5 | -19400 | -91.6 | -25400 | -100.6 | 431.70 | 8200 | 419 | 666.67 | 1.25 |
| DyNi4.25Ga0.75 | AB5 | -28134* | -121.35* | -30100 | -124.71 | 464.24 | 8200 | 419 | 586 | 0.86 |
| DyNi4.5Al0.5 | AB5 | -25334* | -114.67* | -27300 | -118.03 | 440.11 | 8200 | 419 | 586 | 1 |
| ErNi4Al | AB5 | -30414* | -118.86* | -32380 | -122.22 | 429.01 | 8200 | 419 | 586 | 0.9 |
| Er6Fe23 | Misc | -19000* | -75.00* | -19000 | -75 | 2288.00 | 6600 | 500 | 600 | 0.8 |
| EuNi5 | AB5 | -24434* | -125.54* | -26400 | -128.9 | 445.40 | 8200 | 419 | 586 | 1.01 |
| GdNi4.5Al0.5 | AB5 | -30734* | -124.37* | -32700 | -127.73 | 434.86 | 8200 | 419 | 586 | 0.9 |
| HoNi4.5Al0.5 | AB5 | -22134* | -110.57* | -24100 | -113.93 | 442.54 | 8200 | 419 | 586 | 0.9 |
| La0.3Mm0.7Ni4.5Cu0.3Al0.2 | AB5 | -29434* | -115.34* | -31400 | -118.7 | 428.47 | 8200 | 419 | 586 | 1.4 |
| La0.4Pr0.6Co5 | AB5 | -27034* | -119.12* | -29000 | -122.48 | 434.77 | 8200 | 419 | 586 | 0.9 |
| Mm0.8Ca0.2Ni5 | AB5 | -22334* | -105.35* | -24300 | -108.7 | 413.73 | 8200 | 439 | 586 | 1.08 |
| Mm0.9Ti0.1Ni5 | AB5 | -29034* | -121.95* | -31000 | -125.31 | 424.53 | 8200 | 419 | 586 | 1.3 |
| MmNi3.5Cu0.5 | AB5 | -21434* | -92.41* | -23400 | -95.77 | 377.51 | 8200 | 419 | 586 | 1.13 |
| MmNi4.15Fe0.85 | AB5 | -23485* | -101.90* | -25300 | -105 | 431.36 | 8100 | 419 | 586 | 1.14 |
| MmNi4.5Si0.5 | AB5 | -25634* | -106.24* | -27600 | -109.6 | 418.47 | 8200 | 419 | 586 | 0.9 |
| MmNi4.6Al0.4 | AB5 | -25834* | -103.84* | -27800 | -107.2 | 421.09 | 8400 | 419 | 586 | 1.42 |
| MmNi4.6Fe0.4 | AB5 | -29439* | -125.98* | -30447 | -127.7 | 432.64 | 8400 | 419 | 586 | 1.65 |

Continued on next page

Table 2: Low temperature metal hydride selection, extracted from the Purdue Metal Hydride Toolbox [9].

| Name | Type | Absorption | | Desorption | | M | $\rho$ | $C_p$ | $T_k$ | w |
|---|---|---|---|---|---|---|---|---|---|---|
| | | $\Delta H(J/molH_2)$ | $\Delta S(J/molH_2K)$ | $\Delta H(J/molH_2)$ | $\Delta S(J/molH_2K)$ | $(kg/kmol)$ | $kg/m^3$ | $J/kgK$ | $(K)$ | (%) |
| MmNi4.6Sn0.4 | AB5 | -27424* | -112.38* | -29390 | -115.74 | 457.77 | 8200 | 419 | 586 | 0.66 |
| MmNi4Cu0.7Ti0.1Sn0.1Fe0.1 | AB5 | -35334* | -139.66* | -37300 | -143.02 | 441.81 | 8200 | 419 | 586 | 1.4 |
| MmNi4Cu0.7Ti0.1Sn0.1V0.1 | AB5 | -35134* | -137.24* | -37100 | -140.6 | 441.32 | 8200 | 419 | 586 | 1.4 |
| NdNi4.8Sn0.2 | AB5 | -24893* | -101.22* | -25700 | -102.6 | 449.70 | 8200 | 419 | 586 | 1.33 |
| NdNi4.9Sn0.1 | AB5 | -26236* | -106.16* | -27900 | -109 | 443.70 | 8200 | 419 | 586 | 1.34 |
| Pd0.75Rh0.25 | SS | -19400 | -93 | -25400 | -107 | 105.53 | 8200 | 419 | 428.6 | 0.76 |
| Pd0.825Ni0.1Rh0.075 | SS | -16043* | -73.07* | -21400 | -84.4 | 101.37 | 8200 | 419 | 586 | 0.69 |
| PrNi2.5Cu2.5 | AB5 | -17334* | -86.64* | -19300 | -90 | 446.51 | 8200 | 419 | 586 | 0.81 |
| PrNi4.5Fe0.5 | AB5 | -18534* | -81.04* | -20500 | -84.4 | 432.95 | 8200 | 419 | 586 | 1.26 |
| TbNi4.5Al0.5 | AB5 | -24934* | -107.55* | -26900 | -110.91 | 436.54 | 8200 | 419 | 586 | 1.1 |
| Ti0.3Zr0.7Mn2 | AB2 | -17056* | -76.26* | -21000 | -85 | 188.09 | 6700 | 419 | 451 | 0.8 |
| Ti0.85Zr0.15Cr1.2Mn0.8 | AB2 | -21500 | -101 | -26200 | -114 | 160.72 | 6700 | 419 | 361.5 | 2.01 |
| Ti0.85Zr0.15CrMn | AB2 | -20400 | -102.4 | -25300 | -112.1 | 161.30 | 6700 | 419 | 505.2 | 2.07 |
| Ti0.8Zr0.2Mn0.8CrFe0.2 | AB2 | -24056* | -107.43* | -28000 | -116.17 | 163.65 | 6700 | 419 | 451 | 1.8 |
| Ti0.8Zr0.2Mn1.4V0.2Cr0.4 | AB2 | -25056* | -108.45* | -29000 | -117.19 | 164.44 | 6700 | 419 | 451 | 1.9 |
| Ti0.8Zr0.2Mn1.5Cr0.5 | AB2 | -23556* | -101.12* | -27500 | -109.86 | 164.94 | 6700 | 419 | 451 | 2 |
| Ti0.8Zr0.2Mn1.5Fe0.5 | AB2 | -21456* | -94.98* | -25400 | -103.72 | 166.87 | 6700 | 419 | 451 | 1.7 |
| Ti0.95Zr0.05Cr1.2Mn0.8 | AB2 | -16500 | -93.1 | -21900 | -108.1 | 156.38 | 6700 | 419 | 360 | 1.97 |
| Ti0.95Zr0.05CrMn | AB2 | -15100 | -93 | -20800 | -105 | 156.97 | 6700 | 419 | 475 | 1.79 |
| Ti0.95Zr0.05Mn1.55V0.45Fe0.09 | AB2 | -22300 | -95.3 | -28400 | -112 | 163.14 | 6100 | 500 | 365.3 | 1.87 |
| Ti0.98Zr0.02V0.43Fe0.09Cr0.05Mn1.5 | AB2 | -23456* | -103.26* | -27400 | -112 | 160.67 | 5800 | 419 | 451 | 1.90 |
| Ti0.99Zr0.01V0.43Fe0.09Cr0.05Mn1.5 | AB2 | -20120 | -97.4 | -25980 | -112.6 | 160.24 | 8400 | 419 | 385.5 | 1.75 |

Continued on next page

Table 2: Low temperature metal hydride selection, extracted from the Purdue Metal Hydride Toolbox [9].

| Name | Type | Absorption | | Desorption | | M | $\rho$ | $C_p$ | $T_k$ | w |
|---|---|---|---|---|---|---|---|---|---|---|
| | | $\Delta H(J/molH_2)$ | $\Delta S(J/molH_2K)$ | $\Delta H(J/molH_2)$ | $\Delta S(J/molH_2K)$ | $(kg/kmol)$ | $kg/m^3$ | $J/kgK$ | $(K)$ | (%) |
| Ti0.9Zr0.1Fe | AB | -26150 | -101.67 | -28911 | -105.02 | 108.05 | 6500 | 502 | 824.2 | 1.00 |
| Ti0.9Zr0.1MnCr0.9V0.1 | AB2 | -20274* | -95.76* | -22500 | -100.7 | 159.03 | 8200 | 419 | 586 | 1.87 |
| Ti0.9Zr0.2Mn1.6Ni0.2Vf0.2 | AB2 | -15960* | -74.03* | -23190 | -90.06 | 171.64 | 8200 | 419 | 586 | 2 |
| Ti0.9Zr0.2Mn1.8Vf0.2 | AB2 | -20532* | -88.15* | -29150 | -107.26 | 170.89 | 8200 | 419 | 586 | 2 |
| Ti1.1Cr1.2Mn0.8 | AB2 | -24078* | -112.37* | -25100 | -114.64 | 159.00 | 8200 | 419 | 586 | 1.81 |
| Ti1.2Cr1.2Mn0.8 | AB2 | -25575* | -117.18* | -25940 | -117.99 | 163.79 | 8200 | 419 | 586 | 1.93 |
| Ti1.2Cr1.9Mn0.1 | AB2 | -20007* | -100.24* | -20080 | -100.4 | 161.73 | 8200 | 419 | 586 | 1.8 |
| Ti1.2CrMn | AB2 | -24498* | -109.02* | -25520 | -111.29 | 164.37 | 8200 | 419 | 586 | 2.02 |
| Ti1.3Cr1.2Mn0.8 | AB2 | -24954* | -108.08 | -25100 | -108.4 | 168.57 | 8200 | 419 | 586 | 1.9 |
| TiCr1.2Mn0.6 | AB2 | -17467* | -92.96* | -21411 | -101.7 | 143.23 | 8200 | 419 | 586 | 1.6 |
| TiCr1.4Mn0.4 | AB2 | -24356* | -113.26* | -28300 | -122 | 142.64 | 8200 | 419 | 586 | 1.4 |
| TiCrMn0.4Fe0.4V0.2 | AB2 | -20200 | -103 | -22000 | -109 | 154.37 | 8200 | 419 | 300 | 1.90 |
| TiCrMn0.55Fe0.3V0.15 | AB2 | -21000 | -106.8 | -27257 | -125.4 | 154.47 | 8200 | 419 | 336.4 | 1.93 |
| TiCrMn0.7Fe0.2V0.1 | AB2 | -17700 | -101 | -20600 | -107 | 154.58 | 8200 | 419 | 483.3 | 1.95 |
| TiCrMn0.85Fe0.3V0.15 | AB2 | -16956* | -77.45* | -20900 | -86.19 | 170.96 | 8200 | 419 | 586 | 1.6 |
| TiCrMn0.8 | AB2 | -19726* | -102.36* | -23670 | -111.1 | 143.81 | 8200 | 419 | 586 | 1.8 |
| TiCr2 | AB2 | -19056* | -100.39* | -23000 | -109.13 | 151.86 | 8200 | 419 | 586 | 0.8 |
| TiMn1.5V0.45Fe0.1 | AB2 | -18600 | -94.9 | -23100 | -107 | 158.78 | 8200 | 419 | 371.9 | 1.30 |
| TiZr0.02V0.43Fe0.09Cr0.05Mn0.15 | AB | -24291* | -115.81* | -27400 | -122 | 87.46 | 5800 | 419 | 586 | 1.90 |
| V0.855Cr0.145 | SS | -24313* | -114.07* | -29670 | -125.4 | 51.09 | 8200 | 419 | 586 | 0.78 |
| V0.9Cr0.1 | SS | -27993* | -122.67* | -33350 | -134 | 51.05 | 8200 | 419 | 586 | 1.94 |
| YNi4.25Al0.75 | AB5 | -22314* | -95.58* | -24280 | -98.94 | 358.59 | 8200 | 419 | 586 | 1.11 |

Continued on next page

Table 2: Low temperature metal hydride selection, extracted from the Purdue Metal Hydride Toolbox [9].

| Name | Type | Absorption | | Desorption | | M | $\rho$ | $C_p$ | $T_k$ | w |
|---|---|---|---|---|---|---|---|---|---|---|
| | | $\Delta H(J/molH_2)$ | $\Delta S(J/molH_2K)$ | $\Delta H(J/molH_2)$ | $\Delta S(J/molH_2K)$ | $(kg/kmol)$ | $kg/m^3$ | $J/kgK$ | $(K)$ | (%) |
| YNi4.5Al0.5 | AB5 | -20454* | -97.24* | -22420 | -100.6 | 366.52 | 8200 | 419 | 586 | 1.22 |
| Zr0.76Ti0.24Ni1.16Mn0.63V0.14Fe0.18 | AB2 | -29393* | -109.82* | -29700 | -110.5 | 200.69 | 8200 | 419 | 586 | 1.7 |
| Zr0.7Ti0.3Cr0.6Fe1.4 | AB2 | -18056* | -81.72* | -22000 | -90.46 | 187.60 | 8200 | 419 | 586 | 1.5 |
| ZrMo2 | AB2 | -18056* | -96.38* | -22000 | -105.12 | 283.10 | 8200 | 419 | 586 | 1 |
| MmNi4.5Cr0.5 | AB5 | -23534* | -96.67* | -25500 | -100.03 | 430.43 | 8200 | 419 | 586 | 1.2 |
| Ti0.8Zr0.2Mn1.2Cr0.8 | AB2 | -24956* | -103.23* | -28900 | -111.97 | 164.06 | 6700 | 419 | 451 | 2 |
| Ti0.9Zr0.15Mn1.6Cr0.2V0.2 | AB2 | -7629* | -49.14 | -15370 | -66.31 | 165.25 | 6700 | 419 | 451 | 2.1 |
| MmNi4.2Al0.4Co0.4 | AB5 | -26434* | -103.70* | -28400 | -107.06 | 421.19 | 8200 | 419 | 586 | 1.3 |
| TiMn1.5 | AB2 | -21908* | -98.94* | -28700 | -114 | 130.27 | 6400 | 419 | 586 | 1.86 |

End of table

Note: * indicates that these values are calculated by the PMHT and not verified with literature.

Table 3: High temperature metal hydride selection, extracted from the Purdue Metal Hydride Toolbox [9].

| Name | Type | Absorption | | Desorption | | M | $\rho$ | $C_p$ | $T_k$ | w |
|---|---|---|---|---|---|---|---|---|---|---|
| | | $\Delta H(J/molH_2)$ | $\Delta S(J/molH_2K)$ | $\Delta H(J/molH_2)$ | $\Delta S(J/molH_2K)$ | $(kg/kmol)$ | $kg/m^3$ | $J/kgK$ | $(K)$ | (%) |
| Ce0.7La0.7Ni5 | AB5 | -23034* | -101.86* | -25000 | -105.22 | 488.7828 | 8200 | 419 | 586 | 1.4 |
| Er6Fe23 | Misc | -19000* | -75.00* | -19000 | -75 | 2288 | 6600 | 500 | 600 | 0.8 |
| GdNi4.5Al0.5 | AB5 | -30734* | -124.37* | -32700 | -127.73 | 434.86 | 8200 | 419 | 586 | 0.9 |
| La0.3Mm0.7Ni4.5Cu0.3Al0.2 | AB5 | -29434* | -115.34* | -31400 | -118.7 | 428.47 | 8200 | 419 | 586 | 1.4 |
| MmNi4.2Al0.4Co0.4 | AB5 | -26434* | -103.70* | -28400 | -107.06 | 421.19 | 8200 | 419 | 586 | 1.3 |
| MmNi4.5Cr0.5 | AB5 | -23534* | -96.67* | -25500 | -100.03 | 430.43 | 8200 | 419 | 586 | 1.2 |
| Pd0.825Ni0.1Rh0.075 | SS | -16043* | -73.07* | -21400 | -84.4 | 101.3672 | 8200 | 419 | 586 | 0.69 |
| TbNi4.5Al0.5 | AB5 | -24934* | -107.55* | -26900 | -110.91 | 436.5393 | 8200 | 419 | 586 | 1.1 |
| Ti0.3Zr0.7Mn2 | AB2 | -17056* | -76.26* | -21000 | -85 | 188.0901 | 6700 | 419 | 451 | 0.8 |
| Ti0.85Zr0.15Cr1.2Mn0.8 | AB2 | -21500 | -101 | -26200 | -114 | 160.7156 | 6700 | 419 | 361.5 | 2.01 |
| Ti0.8Zr0.2Mn1.2Cr0.8 | AB2 | -24956* | -103.23* | -28900 | -111.97 | 164.06 | 6700 | 419 | 451 | 2 |
| Ti0.8Zr0.2Mn1.5Cr0.5 | AB2 | -23556* | -101.12* | -27500 | -109.86 | 164.9426 | 6700 | 419 | 451 | 2 |
| Ti0.8Zr0.2Mn1.5Fe0.5 | AB2 | -21456* | -94.98* | -25400 | -103.72 | 166.8681 | 6700 | 419 | 451 | 1.7 |
| Ti0.95Zr0.05Mn1.55V0.45Fe0.09 | AB2 | -22300 | -95.3 | -28400 | -112 | 163.1385 | 6100 | 500 | 365.3 | 1.87 |
| Ti0.98Zr0.02V0.43Fe0.09Cr0.05Mn1.5 | AB2 | -23456* | -103.26* | -27400 | -112 | 160.6719 | 5800 | 419 | 451 | 1.90 |
| Ti0.9Zr0.15Mn1.6Cr0.2V0.2 | AB2 | -7629* | -49.14 | -15370 | -66.31 | 165.2516 | 6700 | 419 | 451 | 2.1 |
| TiCrMn0.85Fe0.3V0.15 | AB2 | -16956* | -77.45* | -20900 | -86.19 | 170.9556 | 8200 | 419 | 586 | 1.6 |
| TiMn1.5 | AB2 | -21908* | -98.94* | -28700 | -114 | 130.274 | 6400 | 419 | 586 | 1.86 |
| YNi4.25Al0.75 | AB5 | -22314* | -95.58* | -24280 | -98.94 | 358.5873 | 8200 | 419 | 586 | 1.11 |
| Zr0.7Ti0.3Cr0.6Fe1.4 | AB2 | -18056* | -81.72* | -22000 | -90.46 | 187.5975 | 8200 | 419 | 586 | 1.5 |

Note: * indicates that these values are calculated by the PMHT and not verified with literature.

# 3 State-of-the-art thermally driven metal hydride cooling systems

Research on metal hydride technologies has been carried out since the 1970's. Numerous thermally and compressor driven metal hydride heating and cooling systems have been developed since then. In this chapter the working principle of metal hydride cooling systems is explained and a literature overview of experimental and numerical performances of such systems is given.

## 3.1 Single-stage thermally driven metal hydride cooling systems

A single stage metal hydride cooling system (MHCS) comprises of two pairs of reactors, each pair contains one high temperature hydride reactor and one low temperature hydride reactor. The high temperature reactor, reactor B, is connected to a high temperature level heating circuit that provides the driving force for the process. Typically this heat can be provided by exhaust gasses or other waste heat sources. The low temperature reactor, reactor A, is connected to the low temperature level circuit. The system operates with two periodic half cycles.

During the cooling half cycle, reactor A lowers the temperature in the low temperature cooling circuit to the required level. Desorption of hydrogen is endothermic, and demands heat $\dot{Q}_c$, thus lowering the temperature in the reactor and cooling circuit. The desorbed hydrogen flows to reactor B, where it is absorbed. The absorption reaction is an exothermic reaction, releasing heat $\dot{Q}_{mB}$ to the reactor and heat transfer circuit.

After the cooling half cycle, reactor A will be regenerated with hydrogen with hydrogen released from reactor B. This half cycle is called the regeneration half cycle, when no useful cooling effect is generated. Continuous cooling can be provided by combining two reactor pairs. When one reactor pair is in the regeneration half cycle, the other pair can supply the cooling demand.

### 3.1.1 System layout and control

Figure 4 shows one pair of reactors with their respective heat transfer circuit. The temperature levels of the heat transfer fluids (HTF) in connection with reactor A and B can be controlled with the switches. When the system is in the cooling half cycle, the circuit supplies heat $\dot{Q}_c$ to reactor A at a cold temperature. At the same time, while reactor B is absorbing hydrogen, reactor B will be cooled down by an HTF at ambient temperature and releasing heat $\dot{Q}_{mB}$. If the system is in the regeneration half cycle, reactor A will be in an absorbing state. Reactor A will release heat $Q_m$ at an ambient temperature level. At the same time, hydrogen will be desorbed at reactor B, while demanding heat $\dot{Q}_h$ at a high temperature level.

### 3.1.2 Half cycles

During a half cycle, both reactors move from an initial state (pressure, temperature, and corresponding hydrogen concentration) to a final state. The change of the supply temperature, to the reactors in the two heat exchange circuits at the end of a half cycle, forces the reactors to the new final state. During a half cycle, the temperatures of the reactors change, and so do their corresponding equilibrium pressures. The pressure difference between the gas pressure and the equilibrium pressure in a reactor forces hydrogen to absorb or desorb. The gas pressure

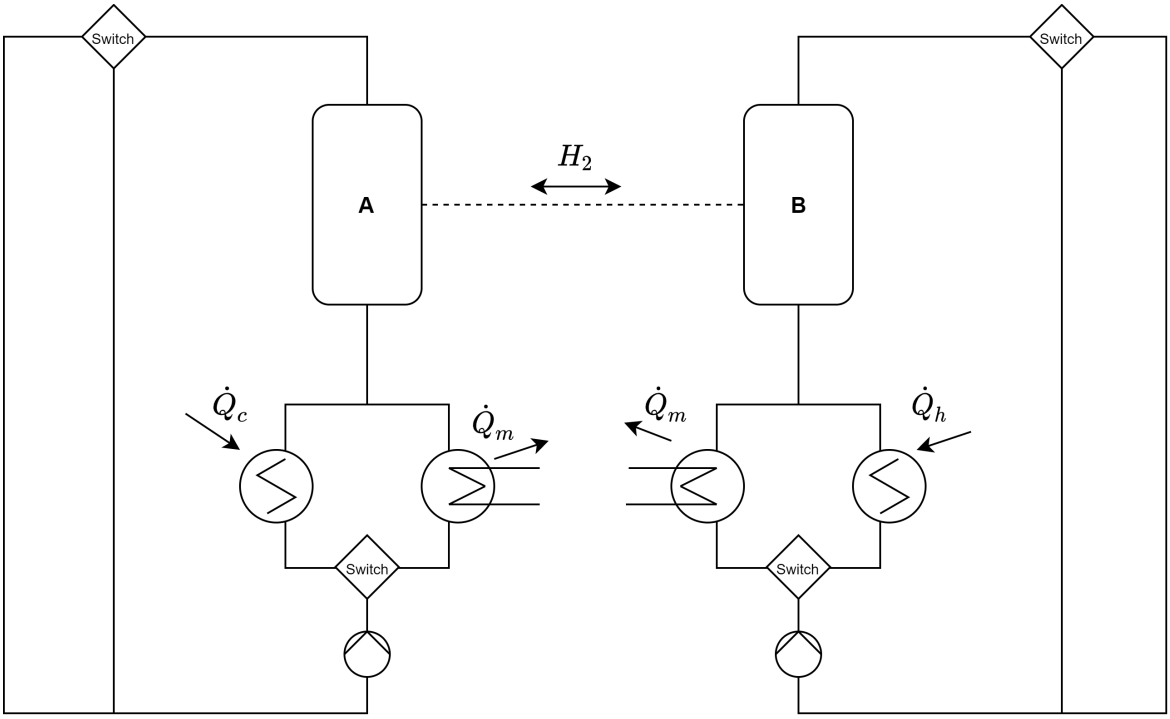


Figure 4: Schematic drawing of the HTF system. The switches in the figure separate the two different temperature levels at the two reactors. The switches coordinate in such a way, that only one temperature level of HTF ($T_c/T_m/T_h$) flows through a reactor at a time. $\dot{Q}_m$ is connected with the ambient temperature level heat exchanger (seawater), $\dot{Q}_c$ is connected with the low temperature level heat exchanger, $\dot{Q}_h$ is connected with the high temperature level heat exchanger (exhaust gases).

difference between reactor A and B forces the hydrogen flow between them. The gas pressure differences between the reactors are relatively small ($< 0.5$ bar). At the end of a half cycle the differences between the equilibrium pressures and gas pressures become small, thus practically stopping the hydrogen exchange. The gas pressure at the end of this half cycle is the initial pressure at the beginning of the next half cycle. Figure 5 shows the average gas pressure and the two equilibrium pressures during a full cycle. The reactors operate between the pressure levels $P_1$ and $P_2$. In the cooling half cycle, the equilibrium pressure in reactor A is higher than the gas pressure in reactor A, forcing hydrogen desorption. At the same time, the equilibrium pressure in reactor B is lower than the gas pressure, forcing absorption. During the regeneration half cycle it will be vice versa.

### 3.1.3 Cooling half cycle

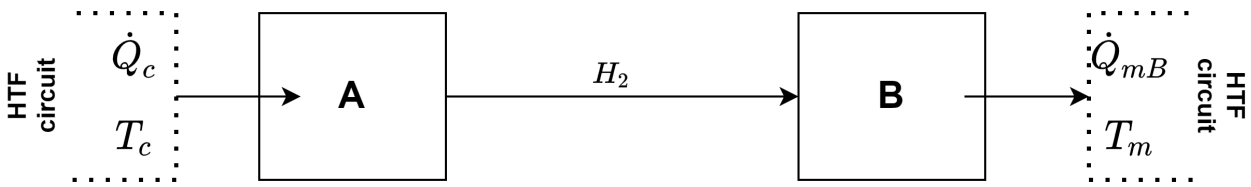


Figure 5: Schematic diagram of a cooling half cycle of a single-stage MHCS. Reactor A has a heat demand $\dot{Q}_c$ at temperature $T_c$, reactor B generates heat $\dot{Q}_{mB}$ at temperature $T_m$

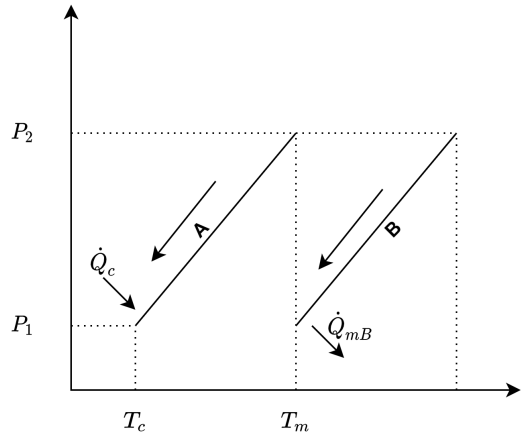


Figure 6: Schematic plot of the thermodynamic cycle (Clausius-Clapeyron plot) of a single-stage MHCS cooling half cycle. The pressure levels in both reactors decrease from $P_2$ to $P_1$.

A single-stage metal hydride system will operate between two pressure levels, a low ($P_1$) and a high ($P_2$) pressure. When the cooling half cycle is initiated, low temperature reactor A will be in a regenerated state, containing a relatively high concentration of hydrogen in the MH alloy. High temperature reactor B will be in a desorbed state, containing a low concentration of hydrogen. At first, both reactors will be at pressure $P_2$, which is the pressure level at the end of the regeneration cycle. At the end of the regeneration, cycle reactor A is at ambient temperature $T_m$ and reactor B at driving temperature $T_h$. To ensure that hydrogen will be desorbed from reactor A and absorbed at reactor B, the temperature of reactor B is lowered to $T_m$ by a heat transfer fluid. Simultaneously reactor A is being cooled down, by a heat transfer fluid as well, to cooling temperature $T_c$. This causes the equilibrium pressures of both MHs to shift in such a way, that the MH alloy present in reactor A has a higher equilibrium pressure than the MH alloy present in reactor B. If the temperature of reactor B is not lowered, but is continuously at $T_h$, the equilibrium pressure of that MH will be higher than the equilibrium pressure of the low temperature alloy present in reactor A, and this will cause the MH alloy to stay in a desorbed state and not able to absorb hydrogen (as the equilibrium pressure of the other MH is lower, absorbing all hydrogen until both equilibrium pressures are equal). The MH alloy having a higher equilibrium pressure will desorb hydrogen, the MH alloy having a lower equilibrium pressure will absorb the released hydrogen. Figure 5 shows the supplied heat $\dot{Q}_c$ at temperature $T_c$ to reactor A and the released heat $\dot{Q}_{mB}$. Figure 8 schematically shows the pressure evolution during operation.

During the cooling half cycle, the low temperature MH will further decrease the temperature in the HTF circuit (lower than $T_c$), creating a cooling effect $\dot{Q}_c$. It is important to note that the HTF flowing into the reactor has temperature $T_c$ and will be cooled down further, as the desorption reaction in reactor A demands heat from the HTF circuit. HTF flowing into reactor B has temperature level $T_m$ and will be heated up by the exothermic absorption reaction.

### 3.1.4 Regeneration half cycle

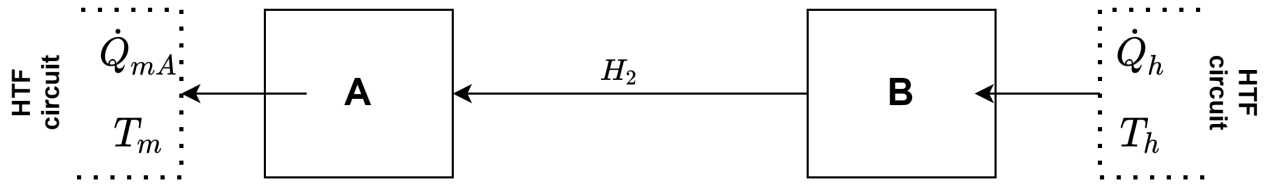


Figure 7: Schematic diagram of a regeneration half cycle of a single-stage MHCS. Reactor A generates heat $\dot{Q}_{mA}$ at temperature $T_m$, reactor B has a heat demand $\dot{Q}_h$ at temperature $T_h$

Hydrogen concentration in MHs influence the equilibrium pressure. The cooling half cycle ends when the equilibrium pressures of both MH alloys have converged to a small pressure difference, causing the MHCS performance to decrease. After the cooling half cycle, the regeneration half cycle must be initiated in order to be able to create a cooling effect.

At the start of the regeneration half cycle, reactor A will be in a desorbed state, having a low hydrogen concentration, and reactor B will have a high hydrogen concentration. Reactor A is at low temperature level $T_c$, reactor B is at ambient temperature level $T_m$. To desorb hydrogen from reactor B and absorb hydrogen at reactor A, the temperature of reactor B needs to rise to $T_h$, to increase its equilibrium pressure above the equilibrium pressure of the MH alloy in reactor A. Heat $\dot{Q}_h$ will be absorbed at reactor B, causing the rise in equilibrium pressure and hydrogen desorption. Simultaneously, in order to not increase the temperature of the cold HTF circuit, reactor A will be cooled by HTF at ambient temperature $T_m$ while absorbing hydrogen, releasing heat $Q_{m1}$. If the MH in reactor A is in a fully absorbed state, the regeneration cycle ends and the cooling half cycle is initiated again.

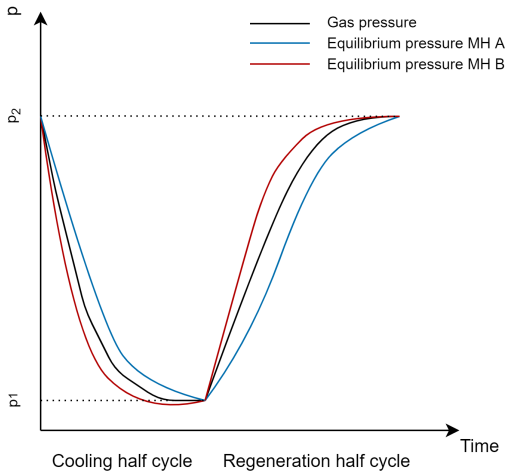


Figure 8: Schematic overview of the pressure levels of an MHCS during a cycle.

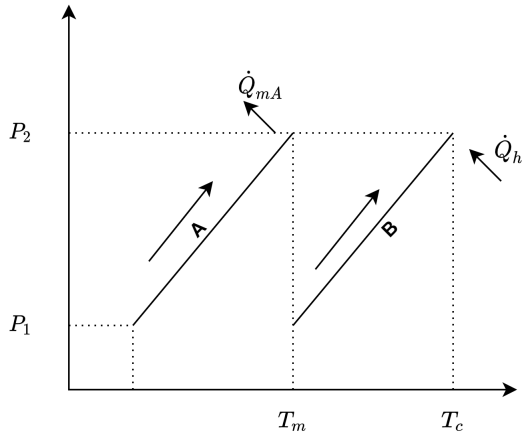


Figure 9: Schematic plot of the thermodynamic cycle (Clausius-Clapeyron plot) of a single-stage MHCS regeneration half cycle. The pressure levels in both reactors increase from $P_1$ to $P_2$.

For a single-stage refrigeration cycle the theoretical coefficient of performance (COP) is defined as:

$$COP = \frac{Q_c}{Q_h} \tag{3}$$

The theoretical COP can also be defined by the enthalpy of formation of the metal hydrides in the system:

$$COP = \frac{\Delta H_{A,des}}{\Delta H_{B,des}} \tag{4}$$

The COP is reduced significantly by sensible heating and cooling of the reactors. These losses may be reduced by internal heat recovery.

#### 3.1.5 Experimental models single-stage systems

Paýa et al. [10] performed experiments with a MHCS and built a numerical model to simulate that system. The cooling temperature was set at 20 °C. A total system specific cooling power (SCP) of 42 W $kg_{MH}^{-1}$ was provided by the system. The COP was calculated to be 0.22. The second law efficiency is low at 0.048, due to a high $COP_{Carnot}$. A relatively short reaction half time of 100 s was reached.

Ron [17] designed an air conditioner model driven by exhaust gases from a bus. The achievable cooling temperature $T_c$ was -2 - 7 °C and a specific cooling power (SCP) of 200 - 250 W $kg_{MH}^{-1}$ (desorbing metal hydride) was achieved. COPs of 0.22 and 0.35 were calculated. The second law efficiencies were between 0.034 - 0.057, due to a high $COP_{Carnot}$.The MHCS reduced the fuel consumption of the bus by up to 30%.

Golben and Huston [18] designed a 2.3 kW metal hydride air conditioner for U.S. Army shelter cooling. The electrical power consumption of 1500 W was almost half of the freon based units (2950 W) they normally used. Power was consumed by circulation of a silicone heat transfer fluid. The practical COP was 1.53 and SCP was 13.9 W $kg^{-1}$. The second law efficiency was 0.16.

Imoto et al. [19] designed an experimental refrigeration system, capable of reaching -20 °C and an SCP of 20 W $kg_{MH}^{-1}$. The system is driven by solar heat of 150 °C. A cycle time of 900-2000 s provides an COP of around 0.45. The second law efficiency was relatively high at 0.23, due to a low $COP_{Carnot}$. The reactors were cylindrical with internal aluminium fins.

Gopal and Murphy [20] carried out experimental studies on an MHCS with two 'tube and coil'-type reactors. The hydrogen was delivered via a single porous tube and the HTF flows through the coils at the outside of the reactor. The SCP was found to be 30-45 W $kg_{MH}^{-1}$. An COP of 0.2 - 0.35 was reached with 5 °C $\leq T_c \leq$ 15 °C. The second law efficiency was at 0.050 - 0.095. Lower temperatures were possible, but as the low temperature reactor used water as HTF this was not feasible.

Qin et al. [21] developed an exhaust gas-driven air conditioner, with the new hydride pair $LaNi_{4.61}Mn_{0.26}Al_{0.13}$/ $La_{0.6}Y_{0.4}Ni_{4.8}Mn_{0.2}$, developed to work at 120 - 200 °C/20-50 °C/-10-0 °C ($T_d/T_m/T_c$). The SCP was 7.7 W $kg_{MH}^{-1}$, with an COP of 0.26. The second law efficiency was 0.050 - 0.33, which is relatively high. This is caused by a low $COP_{Carnot}$ at a cooling temperature of -10 °C and an ambient temperature at 50 °C. Qin et al. note that due to insufficient thermal conductivities in the reactor the design has a long cycle time and low cooling power. Further research needs to be done to increase heat and mass transfer.

Linder et al. [22] published experimental results of a two reactor bed set up, using capillary tube bundle reactor beds, consisting of 372 1.4 mm inner diameter stainless steel tubes. $T_c$ = 20 °C, $T_m$ = 28 °C and $T_d$ = 130 °C. The two reactors contained 1748 g of MH powder and, depending on cooling and ambient temperature, an average SCP of 60 - 780 W $kg_{MH}^{-1}$ was attained. The half-cycle time was in the order of 100 - 120 s. Linder et al. note that the amount of hydrogen needed to cool down the reactor determines the amount of hydrogen available to generate a useful cooling effect. Therefore a decrease in difference between regeneration and cooling temperatures will increase achievable cooling power.

An open thermally driven MHCS consists of a pressurized hydrogen tank, metal hydride reactors and a fuel cell (FC). These systems can utilize part of the potential energy from the pressurized hydrogen before it enters the FC. As an FC typically operates under the pressure levels in an MHCS, it is possible to introduce an intermediary process in which the hydrogen is used to operate a cooling system.
Weckerle et al. (2017) [23] experimentally characterized a novel open single-stage metal hydride cooling system with a half-cycle time of t < 60 s. A plate reactor is used with Hydralloy C5 as hydride material. The system contains a pressure tank at 700 bar, an MHCS and an FC. With this open system it is possible to use part of the potential energy of the pressurized hydrogen before the hydrogen is consumed in the FC. The average SCP = 1.31 kW $kg_{MH}^{-1}$ with $T_c$ = 10 °C during desorption by a single reactor. In continuous operation an average SCP of 690 W $kg_{MH}^{-1}$ was reached at $T_c$ = 10 °C, $T_m$ = 35 °C and a half-cycle time of 60 s. When a maximum temperature difference between $T_c$ and $T_m$ of 7.1 °C was allowed, the SCP increased to 1.7 kW $kg_{MH}^{-1}$ at a half-cycle time of 60 s. Weckerle and his colleagues note that a large benefit, besides the very high SCP, of the plate reactor is the scalability.

Hegner et al. [24] studied a hydrogen based air-conditioning unit used in an FC powered vehicle. The set up included a pressure tank, two metal hydride reactors and an FC with an electric power rating of 8 kW. The cooling power of the cooling system increased with increasing FC power, caused by an increase in hydrogen mass flow. The cooling power was also dependent on the absorption and desorption temperatures, as well as the ambient temperature.

Weckerle et al. (2020a) [25] designed a compact MHCS for air conditioning purposes in automobiles. Four plate reactors were filled with $LaNi_{4.75}Al_{0.25}$ and Hydralloy C5. The weight of the metal hydrides were 1.7 kg and 2.1 kg per reactor, respectively. The half-cycle time showed an optimum, regarding thermal losses, at 210 s and 0.89 kW cooling power, indicating an SCP of 114 W $kg_{MH}^{-1}$. Cooling power increased with a higher driving temperature as it improves regeneration conditions and increases the exchanged hydrogen capacity. Lowering the ambient temperature will increase the maximum amount of hydrogen exchange, due to a lower pressure level in the high temperature reactor. Thermal losses will also decrease due to a smaller temperature difference $\Delta T$. The COP was between 0.15 - 0.20. A second law efficiency of 6.8 $\cdot 10^{-4}$ - 0.037 was obtained. These low second law efficiency are a result of the high calculated $COPs_{Carnot}$. This is an indication that the SCP is a more important measurement of MHCS performance than the second law efficiency is.

Weckerle et al. (2020b) [26] designed a larger version of the plate reactor. 2.92 kg of Hydralloy C2 was distributed over two reactors. A quasi-continuous average cooling power of 662 W was reached at $T_c = 20$ °C and $T_m = 30$ °C, resulting in an SCP of 227 W $kg_{MH}^{-1}$ at an FC power $P_e$ of 5 kW. This is 463 W $kg_{MH}^{-1}$ lower than they reached in Weckerle et al. (2017) [23]. This may be the result of thermal losses from the HTF that is being pumped around the system. Also during the first 20 s of hydrogen desorption, the outlet temperature of the HTF is higher than the inlet temperature, indicating that the reactor itself is still being cooled down and this results in sensible thermal losses.

Table 4 provides an overview of the performance of the MHCS mentioned above.

Table 4: Performance overview of single-stage thermally driven MHCS

| | $T_c$ (°C) | $T_m$ (°C) | $T_d$ (°C) | COP | $COP_{Carnot}$ | 2nd law efficiency | SCP (W $kg_{MH}^{-1}$) | Reaction half time (s) | Metal hydride | Article |
|---|---|---|---|---|---|---|---|---|---|---|
| 1 | 20 | 35 | 130 | 0.22 | 4.61 | 0.048 | 42* | 100 | $LmNi_{4.91}Sn_{0.15}$<br>$Ti_{0.99}Zr_{0.01}V_{0.43}Fe_{0.09}Cr_{0.05}Mn_{1.5}$ | Paýa et al. [10] |
| 2 | -2 - 7 | 35 | 300 - 600 | 0.22 | 3.86 - 6.47 | 0.034 - 0.057 | 250 | 180 | $LaNi_{4.7}Al_{0.3}$<br>$Ni_{4.15}Fe_{0.85}$ | Ron [17] |
| 3 | 32 | 49 | 427 | 1.53 | 9.69 | 0.16 | 13.8* | 600 | $LaNi_{4.5}Al_{0.5}$<br>$(CFM)Ni_5$ | Golben and Huston [18] |
| 4 | -20 | 20 | 150 | 0.45 | 1.94 | 0.23 | 13 - 22 | 900 - 2000 | $LaNi_{4.6}Al_{0.3}Mn_{0.1}$<br>$La_{0.6}Y_{0.4}Ni_{4.8}Mn_{0.2}$ | Imoto et al. [19] |
| 5 | 5 - 15 | 25 - 30 | 110 - 130 | 0.20 - 0.35 | 3.68 - 4.01 | 0.050 - 0.095 | 30 - 45 | 180 - 720 | ZrMnFe<br>$MmNi_{4.5}Al_{0.5}$ | Gopal and Murphy [20] |
| 6 | -10 - 0 | 20 - 50 | 120 - 200 | 0.26 | 0.78 - 5.20 | 0.050 - 0.33 | 7.7 | 3600 | $LaNi_{4.61}Mn_{0.26}Al_{0.13}$<br>$La_{0.6}Y_{0.4}Ni_{4.8}Mn_{0.2}$ | Qin et al. [21] |
| 7 | 20 | 28 | 130 | - | 9.27 | - | 143 - 429 | 100 - 120 | $LmNi_{4.91}Sn_{0.15}$<br>$Ti_{0.99}Zr_{0.43}$ | Linder et al. [22] |
| 8 | 10 | 35 | - | - | - | - | 690 | $< 60$ | $Ti_{0.955}Zr_{0.045}Mn_{1.52}V_{0.43}Fe_{0.12}Al_{0.03}$ | Weckerle et al. [23] |
| 9 | 20 | 30 | - | - | - | - | - | 48-301 | $Ti_{0.98}Zr_{0.02}V_{0.41}Fe_{0.09}Cr_{0.05}Mn_{1.46}$ | Hegner et al. [24] |
| 10 | 16 - 31 | 31.4 | 156.3 | 0.15 - 0.20 | 5.46 - 221.14 | $6.8 * 10^{-4}$ - 0.037 | 60 - 140 | 210 | $LaNi_{4.75}Al_{0.25}$<br>$Ti_{0.955}Zr_{0.045}Mn_{1.52}V_{0.43}Fe_{0.12}Al_{0.03}$ | Weckerle et al. [25] |
| 11 | 20 | 30 | - | - | - | - | 227 | 150 | $Ti_{0.98}Zr_{0.02}V_{0.41}Fe_{0.09}Cr_{0.05}Mn_{1.46}$ | Weckerle et al. [26] |

Note: * indicates the SCP compared with the weight of the total system.

## 3.2 Numerical models metal hydride cooling systems

To design a useful MHCS, credible modelling is required. Many different variables, such as cooling, driving and ambient temperature, enthalpy of formation and equilibrium pressure, as well as reactor geometry impact the capabilities and performance of MHCSs.
In order to reduce the complexity of models and the needed processing time, simplifications and assumptions are made in the models. The following assumptions are made in most numerical models [27]:

- Hydrogen behaves as an ideal gas
- Radiative heat losses are negligible
- There is a local thermal equilibrium (gas and solid have the same temperature)
- Compression work and viscous dissipation is negligible
- Heat transfer by mass convection is negligible
- Dependence of equilibrium pressure on hydrogen concentration is negligible

All models are based on energy and mass balances and some models use intrinsic reaction kinetics of the MH alloys, which are measured in experiments.

## 3.3 Some heat and mass transfer considerations

The operation characteristics of MHCS are determined by the heat and mass transfer processes, associated with the release and uptake of heat and the absorption and desorption of hydrogen in the metal hydride. The reaction kinetics of metal hydrides is usually fast, therefore high heat and mass transfer coefficients are desired in these systems. Sufficient heat and mass transfer is essential to prohibit the system of coming to a standstill, because of heating or cooling down the reactors above or below the equilibrium pressure of the metal hydride. To ensure appropriate mass transfer porous tubes are placed in metal hydride reactors. Hydrogen supply is, by using this technique, uniform in the axial direction and only needs to diffuse over a relatively small thickness of metal hydride in the radial direction.

Usually thermally very well conducting foam matrices, such as aluminium or copper foams, are placed in the reaction bed to enhance thermal conductivity. Recently Linder et al. [22], Paýa et al. ([10, 11, 28]) and Weckerle et al. [26, 23, 25] proposed novel designs that do not need to implement such matrices, but use enhanced reactor designs (capillary tube and plate reactor) that allow for larger systems. These type of solutions allow for short cycle times for absorption and desorption of hydrogen. By shortening the cycle time the SCP will increase, if the amount exchanged hydrogen stays constant [5].

Linder [7] showed that the cycle time of metal hydride systems is limited by the intrinsic reaction kinetics during desorption. As these kinetics are dependant on reaction temperature, lowering the temperature will further decrease the reaction speed. Linder discusses that decreasing the half-cycle time of MHCS is not possible

by further increasing reaction bed characteristics but only by implementing faster metal hydride desorption reaction kinetics.

### 3.4 Numerical models single-stage systems

Nishizaki et al. [29] first proposed a model for calculating the COP of a metal hydride heat pump. The model includes the sensible heat exchange between reactors and design parameters, such as the PCT properties, heat capacities and efficiency of sensible heat exchange. In the study it was determined that a small pressure slope in the $\alpha+\beta$-phase, narrow hysteresis and a low sensible heating is necessary to obtain sufficiently high COP values.

Mellouli et al. [30] used their zero-dimensional model to determine the ideal operating temperatures in a metal hydride heat pump using $MmNi_{4.5}Al_{0.5}$ / $MmNi_{4.2}Al_{0.1}Fe_{0.7}$ as a hydride pair. The steady model states that the convection term is negligible due to a high volumetric heat transfer coefficient. The COP and SCP of the MHHP varied between 0.45 - 0.50 and 45 - 120 W $kg_{MH}^{-1}$, depending on the operating temperatures in the range of 52-67 °C / 0-20 °C / -23 - -8 °C ($T_d$, $T_m$, $T_c$).

Shatheesh [8] performed studies on reaction kinetics, heat and mass transfer models and the performance of single and double-stage metal hydride heat pumps. He showed that the so called Jander diffusion model closely resemble the experimental data for three different metal hydride alloys. He also concluded that the SCP and COP of metal hydride heat pumps will increase with heat source and cooling temperatures and will decrease with heat sink temperature. Furthermore, Shatheesh notes that the influence of the heat source and the cooling temperature are more notable than the heat sink temperature.

Paya et al. [10, 28] performed simulations on the experimental set-up used by Linder et al. [22]. The model was developed on a basis of a set of differential and algebraic equations (DAE). The equations were implemented in MATLAB and SIMULINK. The intrinsic reaction kinetics show a large difference under dynamic and static PCT conditions, but are well defined within the model and therefore lead to an accurate prediction of hydrogen exchange rate between the reactors. The model calculates the hydrogen mass flow rate precisely and is a 'clear improvement with respect to literature on the modelling of MHCS'. The model does not include a convection term, as it states that hydrogen gas velocity is very low and is at a moderate temperature. The equilibrium pressure is calculated by a modified Van't Hoff equation. Also, Paya and colleagues proved that a high heat source temperature, a high cooling temperature, a specifically determined cycle time (100-120 s) and a specific initial hydrogen (1.31 wt%) concentration all increase the performance of this system, compared to improving the heat transfer.

Sharma et al. (2015) [31] used dynamic and static PCT data of hydride pair $La_{0.9}Ce_{0.1}Ni_5$ / $LaNi_{4.7}Al_{0.3}$ to indicate the difference in results after a thermodynamic analysis. In conventional analyses the pressure and concentration at the middle of the pressure plateau is used for thermodynamic analysis. In dynamic modelling the pressure and concentration is allowed to continuously change. The model shows that static P-C-T data tends to over-predict the COP of this MHCS by 31.9%.

Weckerle et al. (2019) [32] propose an improved plate reactor design compared to the original designed by them [23]. Several optimisations are discussed, such as a more efficient channel diameter and decreased pressure drop. An COP increase of up to 60%, compared to the original plate reactor, may be possible. A 2 D model is proposed in the article and shows very realistic results compared to experiments. The geometry of the reactor is used in the model, which is not the case in the models previously discussed.

Table 5 shows the important terms used in the recent models mentioned above.

Table 5: Overview of terms of numerical models

| Article | Hydrogen mass transfer | Unsteady term | Convection term | Conduction term | Heat flow term | Dimension | Reactor type |
|---|---|---|---|---|---|---|---|
| [8] | $\dot{m} = \zeta \frac{\delta(\rho_g)}{\delta t} + \nabla(\rho_g \vec{u_g})$ * | $\dot{m}_A \frac{\Delta H}{m_g}$ | $\vec{u}_g \cdot \nabla T$ | $\lambda_{eff} \nabla^2 T$ | $\dot{Q} = \dot{m}_{HTF} C_{p,HTF} (T_{HTF,o} - T_{HTF,i})$ | 2 D | Conventional |
| [30] | $a \frac{dx}{dt}$ ** | $\frac{dm_g}{dt} \Delta H$ | - | - | $\dot{Q} = \dot{m}_{HTF} \cdot C_{p,HTF} (T_r - T_{HTF,i})(1 - e^{NTU})$ | O D | Conventional |
| [10, 11, 28] | $\frac{dm_g}{dt} = -\frac{m_A}{100} \cdot \frac{dw}{dt} + \dot{m}_i - \dot{m}_o$ | $\frac{\Delta H}{MH_2} \frac{m_A}{dt} \frac{dw_A}{dt}$ | - | - | $\dot{Q}_w = \epsilon \cdot \dot{m}_w \cdot C_{p,w} \cdot (T_{w,i} - T_{mm})$ | O D | Capillary tube |
| [32] | $\frac{\delta(\zeta \rho_g)}{\delta t} + \nabla(\rho_g u) = -(1-\zeta)\rho_s \frac{\delta m_{H2}}{\delta t}$ * | $\frac{(1-\zeta)\rho \Delta H}{M_{H_2}} \frac{\delta w}{\delta t}$ | $\vec{u}_g \cdot \nabla T$ | $\nabla(-\lambda_{eff} \nabla T)$ | $\dot{Q} = \alpha_{MH} A (\Delta T)$ | 2 D | Plate |

* Note: $\zeta$ is the porosity (void fraction) of the metal hydride powder. ** Note: Parameter 'a' links the hydrogen flowing from the bed per mole MH and has unit kg, $dX/dt$ has unit mol/mol / s.

# 4 Selection of metal hydride alloys for refrigeration purposes

## 4.1 PCT characteristics model

A precise PCT characteristics model is an important part of an MHCS, as the pressure, equilibrium pressure, hydride concentration and temperature are all parameters that have an influence on the intrinsic reaction kinetics of an MH and therefore on the performance of an MHCS.

The PCT characteristics model used in this research is based on the modified Van't Hoff equation:

$$ln\ P_{eq} = -\frac{\Delta H}{RT} + \frac{\Delta S}{R} + f_s(w - w_{mid}) \tag{5}$$

This equation is a modified version of the original Van't Hoff equation. It takes the non-negligible slope in the $\alpha + \beta$ region into consideration.

To obtain the constants in the modified Van't Hoff equation, the pressure and temperature are measured for an MH at a certain concentration. The reference pressure is taken at 1 bar. $w_{mid}$ is the concentration at the middle of the plateau region ($\alpha + \beta - region$). In figures 10 and 11 the PCT characteristics, obtained from the PHMT, of the two MH alloys used in numerical model presented in chapter 5. Notice the small differences in the enthalpy and entropy values when comparing the values from table 6 to the values displayed in figures 10 and 11, caused by measurement errors. In the model the values given by Paýa [10, 11, 28] are taken, as they are more recently derived from experiments, than the data used by Shatheesh et al. [33], which is the source the PHMT refers to. Paýa [11] showed that the modified Van't Hoff equation can accurately model the plateau region. In the following table the fitting parameters of the alloys $Ti_{0.99}Zr_{0.01}V_{0.43}Fe_{0.09}Cr_{0.05}Mn_{1.5}$ and $LmNi_{4.91}Sn_{0.15}$ are given. These two alloys are, respectively, the low temperature and high temperature alloys used to validate (see chapter 6) the numerical model presented in chapter 5.

After the model has been validated, a new low temperature MH will be added to the model in order to achieve a

Table 6: Parameters used in the modified Van't Hoff equation and the mass present in the reactors.

| Alloy | Mass MH (kg) | abs/des | $\Delta H$ $(J/molH_2)$ | $\Delta S$ $(J/molH_2K)$ | fs | $w_{mid}$ (w/w%) |
|---|---|---|---|---|---|---|
| $Ti_{0.99}Zr_{0.01}V_{0.43}Fe_{0.09}Cr_{0.05}Mn_{1.5}$ | 0.831 | abs | 19989 | 97 | 0.423 | 0.97 |
| | | des | 25477 | 111 | 0.215 | |
| $LmNi_{4.91}Sn_{0.15}$ | 0.948 | abs | 27170 | 103 | 0.428 | 0.65 |
| | | des | 31026 | 113 | 0.475 | |
| $Ti_{0.95}Zr_{0.05}Cr_{1.2}Mn_{0.8}$ | 0.831 | abs | 16500 | 93.10 | 0.395 | 0.98 |
| | | des | 21900 | 108.10 | 0.398 | |

lower cooling temperature, needed for the ice slurry machine to function. The MH alloy $Ti_{0.95}Zr_{0.05}Cr_{1.2}Mn_{0.8}$ is selected, from the PMHT database, which extracted the data from Vanhanen et al. [34], as a potential candidate to replace the low temperature MH alloy in the model. Figure 12 displays the PCT characteristics of this alloy. As can be seen, the proposed MH has a higher equilibrium pressure at low temperatures, than the original low temperature MH. This will increase the systems ability to perform at lower temperatures. For an alloy combination, it is essential the high temperature alloy has a higher equilibrium pressure during the regeneration half cycle than the low temperature alloy. For the cooling half cycle it is essential that the low

temperature alloy has a higher equilibrium pressure, otherwise adsorption and desorption cannot occur in the desired direction.

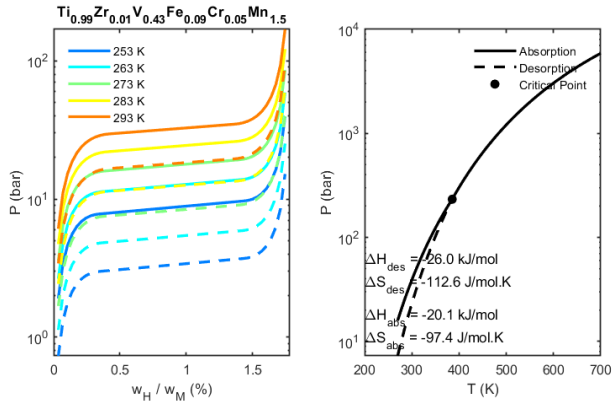


Figure 10: PCT characteristics of low temperature MH alloy $Ti_{0.99}Zr_{0.01}V_{0.43}Fe_{0.09}Cr_{0.05}Mn_{1.5}$, obtained from the PMHT [9]. Note that the values in this figure differ from the values presented in table 6.

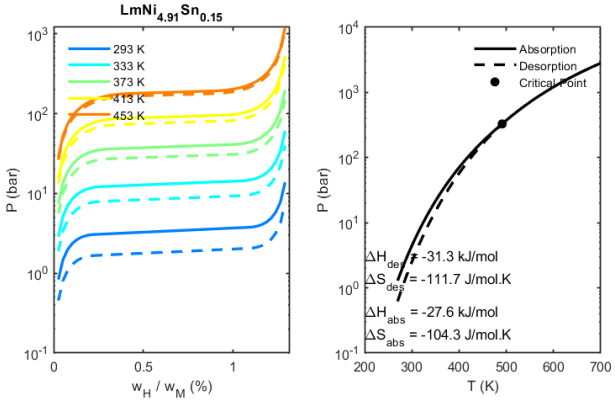


Figure 11: PCT characteristics of high temperature MH alloy $LmNi_{4.91}Sn_{0.15}$, obtained from the PMHT [9]. Note that the values in this figure differ from the values presented in table 6.

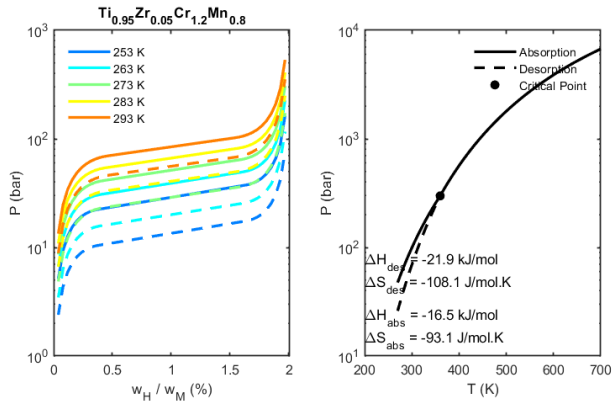


Figure 12: PCT characteristics of $Ti_{0.95}Zr_{0.0}5Cr_{1.2}Mn_{0.8}$, obtained from the PMHT [9]. This MH alloy is introduced into the model to obtain lower cooling temperatures.

# 5 Heat and mass transfer model

## 5.1 Introduction

The equations of the heat and mass transfer model will be numerically solved for the simulation of heat and mass transfer characteristics between the metal hydride reactors and the heat transfer fluid. The model will be implemented in MATLAB and will be discussed below.

The performance of a closed MHCS is depends on the thermodynamic properties of an MH alloy (intrinsic reaction kinetics, equilibrium pressure, hydride concentration, hysteresis etc.) and the heat and mass transfer properties of the system. Each part of an MHCS can be modelled by differential equations and therefore a dynamic model is needed to simulate the behaviour of such a system.

Especially one variable of the system is important to be defined properly and that is if a spatial model is required in the simulation. There are 0 D, 1 D, 2D and 3D models of MH reactors during absorption or desorption [3, 35, 29, 30, 10, 28, 32, 11].

In this work, based on Paýa [11], the model is 0 D as the heat transfer characteristics of the reactor does not limit the overall performance of the system. Besides this point, the goal of the simulation is to predict the global system performance and therefore the small temperature differences in the reactor beds do not have to be taken into account directly. Because of this, the temperature of the MH reactor bed is taken to be uniform in the axial and radial direction.

The model presented in this thesis is partly based on the reactor geometries Paýa used in his dissertation [10, 11]. Values of certain parameters are unclear from his work and are therefore taken to realistic values.

## 5.2 Model assumptions

As discussed in section 3.2 numerical models make certain assumptions to decrease the computation time of the model. The assumptions can be made as the influence of these parameters will be negligible compared to other parameters in the system. The model used in this thesis is inspired by the PhD dissertation of Paýa [11] and will be implemented in SIMULINK. The following assumptions have been made in this numerical model:

- Hydrogen acts as an ideal gas
- The transport properties of the hydrogen gas are independent of temperature, hydrogen concentration and pressure.
- The tube bundle configuration shows excellent heat transfer characteristics and therefore it has been assumed that the MH reactor has a quasi-uniform temperature distribution (heat transfer to and from the HTF has been modified to the uniform model, see equation 10).
- Heat transfer by convection and radiation within the MH powder is neglected, due to low gas velocity and moderate temperature differences.
- The intrinsic reaction kinetics are modelled considering the difference between the actual pressure and the equilibrium pressure is the driving force of hydrogen absorption and desorption.

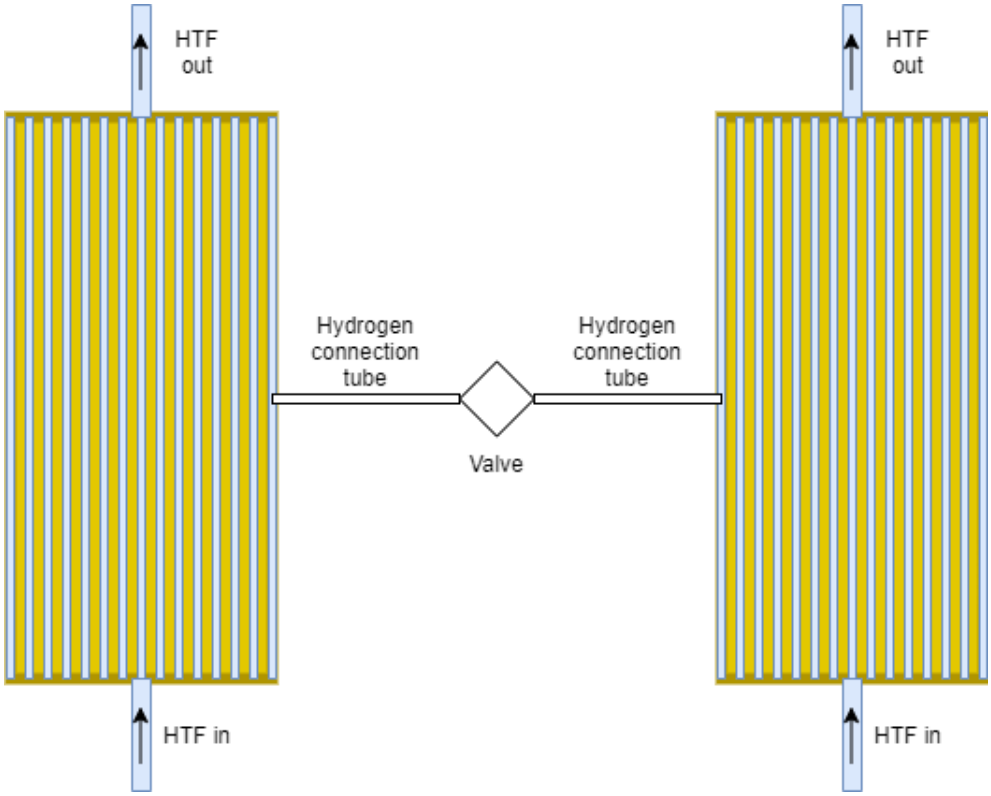


Figure 13: Schematic drawing of the MH reactor system setup

- Hydrogen enters the bed through a filtered tube. The diffusion of hydrogen through this filter and the MH power does not limit the reaction rate.
- The heat transfer characteristics of the MH powder is independent on pressure, temperature and hydrogen concentration.

## 5.3 System geometries

The reactors, implemented into the proposed model, have certain geometries and have an influence on the behaviour and performance of the system, f.e. the mass of MH powder, tube length and connection tube area. In the table below, a summary has been given of the values of these geometries and characteristics.

## 5.4 Formulation of equations

### 5.4.1 Reaction kinetics

In this numerical model, the differences between the pressures in the reactors and the static equilibrium pressures are the driving forces of the sorption processes. The amount of hydrogen that flows from a reactor bed depends on the temperature and pressure in that bed, as well as the hydrogen concentration.

$$\frac{dw}{dt} = K\ e^{-\frac{E}{RT}}\ \frac{P_g - P_{eq}(T,w)}{P_{eq}(T,w_{\alpha+\beta\rightarrow\beta}) - P_{eq}(T,w_{\alpha\rightarrow\alpha+\beta})} \tag{6}$$

Table 7: Values of parameters implemented into the model.

| Parameter | Value |
|---|---|
| Metallic mass | 2 kg |
| Low temperature MH A | 0.831 kg |
| High temperature MH B | 0.948 kg |
| Volume reactors | 0.7 L |
| $n_{tubes}$ | 372 |
| HTF tube length | 0.123 m |
| External diameter HTF tube | 0.0018 m |
| Internal diameter HTF tube | 0.0014 m |
| Distance tubes (S) | 0.0018 m |
| Hydrogen connection tube area | 2.2566e-05 $m^2$ |
| Volumetric flow rate HTF | 4 L/min |
| $C_{p,MH}$ | 355 J/kgK |
| $C_{p,mm}$ | 500 J/kgK |
| $UA_{MH,A}$ | 559.9 W/K |
| $UA_{MH,B}$ | 605.6 W/K |
| $h_m$ | 5 W/$m^2$K |

The equilibrium pressure will be calculated at each time step. $w_{\alpha+\beta\rightarrow\beta}$ and $w_{\alpha\rightarrow\alpha+\beta}$ make reference to the right and left limit of the plateau region of the MH. Reaction rate constant K and reaction activation energy E are determined during experiments and have different values for different MHs, as well as different values during absorption or desorption.

As can be seen from equation 6, hydrogen flows from the reactor bed if the gas pressure is lower than the equilibrium pressure and flows into the bed if the gas pressure is higher.

### 5.4.2 Energy equation

The variation of the internal energy in the MH reactors are modelled through a number of different equations. As was mentioned in the assumptions list, the model is a zero-dimensional model and therefore is a lumped model. The internal energy in the MH powder is evaluated by equation 7. The left term of the equation takes the change in temperature of the MH into account. The first term on the right side of the equation states that the absorption/desorption of hydrogen will bring forward a temperature change in the powder. The second term on the right takes into account the different gas temperatures between the high temperature and low temperature reactors. This factor will change to zero for the desorbing reactor, as no transport from the absorbing to the desorbing reactor will take place. The last term states that a temperature difference between the metal tubes that carry the HTF and the bulk MH powder will contribute to a change in temperature of the powder.

$$C_{p,MH} m_A \frac{dT_A}{dt} = \frac{\Delta H \; m_A}{MH_2} \frac{dw_A}{dt} + \dot{m}_i \; C_{p,H_2}(T_B - T_A) + UA_{MH}(T_{mmA} - T_A) \tag{7}$$

Where, according to Mills [36],

$$UA_{MH} = \frac{2 \; \pi \; \lambda_{MH} \; L \; n_{tubes}}{ln\left(\frac{De+S}{De}\right)} \tag{8}$$

Figure 14 and 15 schematically show the capillary tube reactor configuration and the HTF tube distribution.

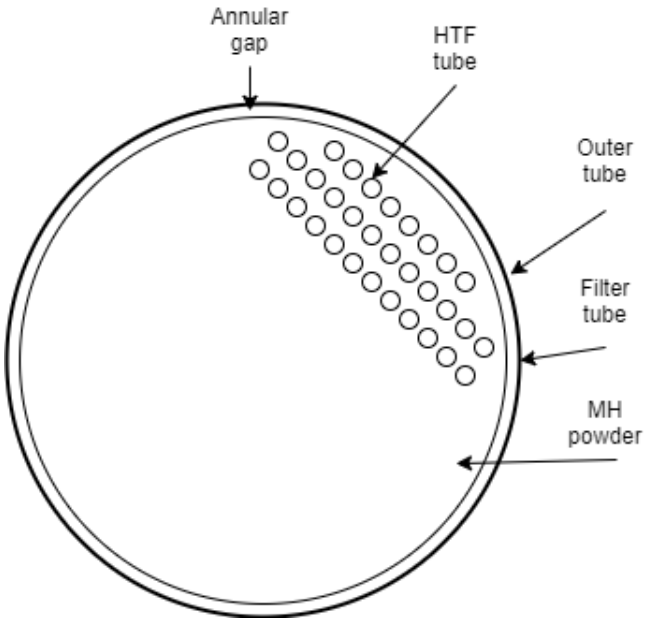


Figure 14: Schematic drawing of the inside of the capillary tube MH reactor

The energy change of the metal tubes in the reactor is calculated by an energy balance, which is written as:

$$C_{p,mmA} m_{mm} \frac{dT_{mmA}}{dt} = -UA_{MH}(T_{mmA} - T_A) + \dot{Q}_{wA} + h_m A_{mm}(T_m - T_{mmA}) \tag{9}$$

The model is zero-dimensional, but as the HTF temperature will not be uniform along the tubes the heat transferred to the HTF circuit is estimated with $\dot{Q}_{wA}$.

$$\dot{Q}_{wA} = \epsilon_A \dot{m}_{wA} C_{p,w}(T_{wAi-T_{mmA}}) \tag{10}$$

The effectiveness of the heat exchanger is calculated by the following equations, assuming the metallic tube temperature is uniform:

$$UA_w = \pi D_i L h_w n_{tubes} \tag{11}$$

$$NTU = \frac{UA_w}{(\dot{m}\ C_p)_{min}} \tag{12}$$

$$\epsilon = 1 - e^{-NTU} \tag{13}$$

Lastly, the temperature of the HTF flowing from the reactors is calculated by using the following equation:

$$C_{p,w}\ m_w \frac{dT_{wAo}}{dt} = \dot{m}_{w,A} C_{p,w}(T_{wAi} - T_{wAo}) - \dot{Q}_{wA} \tag{14}$$

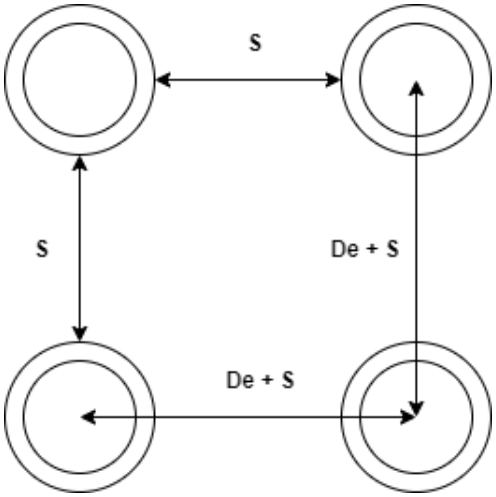


Figure 15: Schematic drawing of the tube distribution in the capillary tube MH reactor

### 5.4.3 Hydrogen mass balance and flow

The mass balance equation [10, 11] is derived from a mass balance of the hydrogen gas in the reactors and is dependent on the amount of hydrogen absorbed or desorbed in the reactor and the mass flow between the reactors.

$$\frac{dm_{gas,A}}{dt} = -\frac{m_A}{100}\frac{dw_A}{dt} + \dot{m}_{Ai} - \dot{m}_{Ao} \tag{15}$$

The mass flow between the reactors is calculated with the Bernoulli equation and is given by the following set of equations:

$$\dot{m}_{Ai} = \begin{cases} \Omega\ \sqrt{2\ \rho_{H2,B}(P_B - P_A)}, & \text{if } P_B \geq P_A \\ 0, & \text{otherwise} \end{cases} \tag{16}$$

$$\dot{m}_{Bi} = \begin{cases} \Omega\ \sqrt{2\ \rho_{H2,A}(P_A - P_B)}, & \text{if } P_A \geq P_B \\ 0, & \text{otherwise} \end{cases} \tag{17}$$

$$\begin{aligned} \dot{m}_{Ai} &= \dot{m}_{Bo} \\ \dot{m}_{Bi} &= \dot{m}_{Ao} \end{aligned} \tag{18}$$

Where $\Omega$ is the mass flow area of the hydrogen connection line present between the reactors.

### 5.4.4 Hydrogen gas pressure

The hydrogen gas pressure inside the reactors is calculated with the ideal gas equation, rewritten as a differential equation. The pressure change is dependent on the changes of temperature and gas mass in the reactors. The

temperature of the hydrogen is assumed to be equal to the reactor temperature.

$$P = \frac{mRT}{MH_2V} \tag{19}$$

$$\frac{dP}{dt} = \frac{RT}{MH_2V}\frac{dm}{dt} + \frac{mR}{MH_2V}\frac{dT}{dt} \tag{20}$$

$$\frac{dP}{dt} = P\left(\frac{1}{m_g}\frac{dm_g}{dt} + \frac{1}{T}\frac{dT}{dt}\right) \tag{21}$$

### 5.4.5 PCT characteristics

The PCT equilibrium characteristics of MHs can be calculated using different models, as presented in chapter 4. In this model the modified Van't Hoff equation is used, as it is fairly simple but accurate. The equation accounts for the slope in the $\alpha + \beta$-region. The other models used in literature are more complex as there are much more fitting parameters involved in the models than in the modified Van't Hoff model, while not necessarily being more accurate.

As described above by equation 5, the equilibrium pressure in this model is calculated by the modified Van't Hoff equation.

$$lnP_{eq} = -\frac{\Delta H}{RT} + \frac{\Delta S}{R} + f_s(w - w_{mid}) \tag{22}$$

The model by Paýa uses another version of the equilibrium pressure, accounting for the equilibrium pressure increase or decrease outside of the $\alpha + \beta$-region. In the model described in this thesis it is assumed that the equilibrium pressure change just outside of this region is negligible for the overall system performance prediction.

During desorption the gas pressure in a reactor will be lower than the equilibrium pressure of the MH present in that reactor. If a reactor is in an absorbing state the gas pressure will be higher than the equilibrium pressure of the MH. The equilibrium pressures of MHs differ, when the MH is absorbing or desorbing. This difference in pressures is called hysteresis and will cause a decrease in performance. An MH will have a higher equilibrium pressure during absorption compared to the equilibrium pressure at during desorption. To take the hysterisis in the model into account, some modifications during the switching between absorption and desorption need to be made, so that the equilibrium pressure increase or decrease is not instantaneously achieved. The model accounts for hysteresis by implementing a transition process [10, 11].

When the model changes from desorption to absorption the following equation is used to achieve a smooth transition between the MH PCT characteristics:

$$P_{eq} = P_{eq,des} + x^2\ (P_{eq,abs} - P_{eq,des}) \tag{23}$$

Where

$$x = \frac{t - t_0}{\Delta t_{trans}} \tag{24}$$

$t$ is the time, $t_0$ is the time when the transition phase starts and $\Delta t_{trans}$ is the total time needed for the transition between absorption and desorption. Paýa [11] indicates that a time of 9 s for the transition phase is required for a smooth transition.

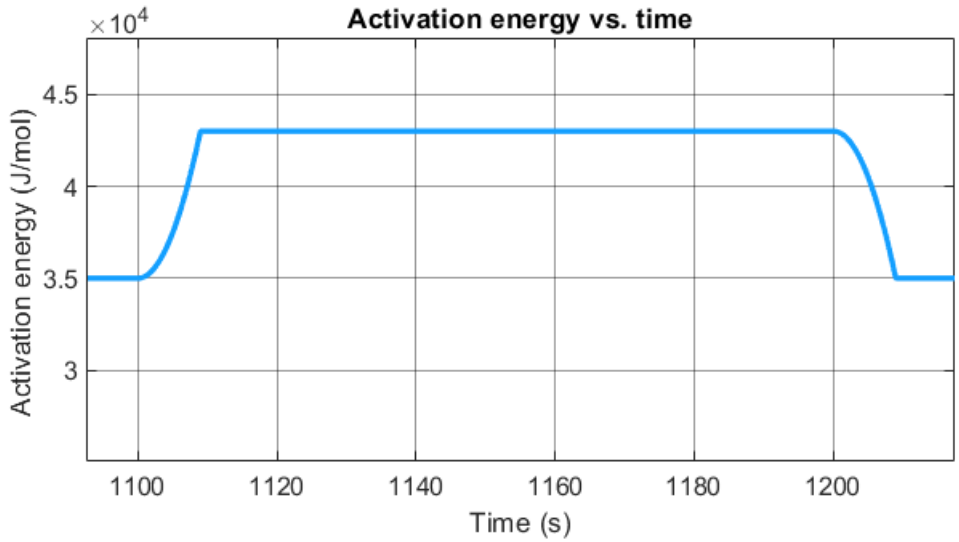


Figure 16: Activation energy (J/mol) vs. time (s)

When a reactor transitions from absorption to desorption the transition equation is as follows:

$$P_{eq} = P_{eq,abs} + x^2 \ (P_{eq,des} - P_{eq,abs}) \tag{25}$$

The transition equation is also used for the parameters used in the kinetic equation, to ensure a smooth transition between absorption and desorption. Figure 16 shows the effect of the transition equation on the reaction activation energy $E$.

### 5.4.6 Model solving

The set of equations, described above, is implemented in SIMULINK and solved by the differential equation solver ode23tb, with a maximum step size of 0.1 s. The system is stiff due to the pressure calculation and therefore is solved implicitly by ode23tb. To compare the numerical results obtained by this model with the results obtained by Paýa [10, 11], the model has different types of inputs:

Table 8: Model inputs

| |
|---|
| Initial conditions: |
| $T_{A0}, T_{B0}, w_{A0}, w_{B0}, P_{A0}, P_{B0}$ |
| Time dependent HTF inputs: |
| $T_{wAin}, T_{wBin}, \dot{m}_{wA}, \dot{m}_{wB}$ |
| Time dependent metal hydride parameters: |
| $\Delta H, \Delta S, f_s, K, E$ |
| Constant parameters: |
| $m_{MH}, m_{mm}, UA_{MH}, S, UA_w, m_w, V, \epsilon$ |

# 6 Validation of the numerical model

In this section the MHCS model will be validated by comparing the simulation results to the simulation and experimental results obtained by Paýa et al. [10, 11].

## 6.1 Cooling and regeneration half cycle

The MH alloy $Ti_{0.99}Zr_{0.01}V_{0.43}Fe_{0.09}Cr_{0.05}Mn_{1.5}$ is present in low temperature reactor A and $LmNi_{4.91}Sn_{0.15}$ is present in high temperature reactor B. Reactor A is initially fully hydrated at 48 bar and 1.1 w/w% hydrogen concentration. The initial temperature of both reactors in the simulation are $T_m = 29°C$. Reactor B is initially in a desorbed state at 10 bar and 0.3 w/w% hydrogen concentration. When the cycle starts the low temperature HTF ($T_c = 18°C$) flows into reactor A, while absorbing reactor B is cooled by a HTF at $T_m = 29°C$. This cooling half cycle duration is 100 s and the system then enters into a regeneration half cycle, of which the duration is also 100 s. During this next phase, desorbing reactor B is heated up by the HTF at $T_h = 130°C$ and absorbing reactor A is cooled down at HTF temperature $T_m = 29°C$. The heat generated (i.e. absorption enthalpy) at reactor A is dissipated to a heat exchanger at ambient temperature.
When the cooling half cycle is initiated, the pressure decreases in both reactors, caused by the temperature decrease in both reactors. The differences in gas pressures and the equilibrium pressures are the driving potentials of this system and allows hydrogen desorption from reactor A and absorption at reactor B. At the beginning of the cooling half cycle, the equilibrium pressure in reactor B drops, as well as the equilibrium pressure in reactor A. Half way through the half cycle the equilibrium pressure in reactor A keeps declining (as the hydrogen concentration in the MH decreases) and the equilibrium pressure in B rises, slowly decreasing the system performance. When the cooling half cycle ends, the regeneration cycle is initiated. The temperature in both reactor beds rises. If the hydrogen gas pressure and equilibrium pressure in bed B are greater than the pressure in bed A, the hydrogen will flow from reactor B to reactor A, regenerating reactor A with hydrogen.

Table 9: Initial values implemented into the model and temperature levels.

| Parameter | (Initial) value |
|---|---|
| $T_A$ | $29°C$ |
| $T_B$ | $29°C$ |
| $P_A$ | 48 bar |
| $P_B$ | 10 bar |
| $w_A$ | 1.1 w/w% |
| $w_B$ | 0.4 w/w% |
| $T_c, T_m, T_h$ | $18, 29, 130°C$ |
| $t$ (half cycle) | 100 s |

## 6.2 Performance analysis

The reactor pressure obtained from the model is shown in figure 17. The model produces a pressure between 48 and 10 bar in the reactors. This is higher than Paýa [11] obtained in his dissertation, see figure 18. The

Table 10: Metal hydride parameters and their corresponding values.

| Parameter | Value |
|---|---|
| $K_{A,abs}$ | $3 \cdot 10^8$ |
| $K_{A,des}$ | $9 \cdot 10^4$ |
| $K_{B,abs}$ | $1.52 \cdot 10^5$ |
| $K_{B,des}$ | 294 |
| $E_{A,abs}$ | 35000 $J/mol$ |
| $E_{A,des}$ | 53000 $J/mol$ |
| $E_{B,abs}$ | 43651 $J/mol$ |
| $E_{B,des}$ | 28976 $J/mol$ |

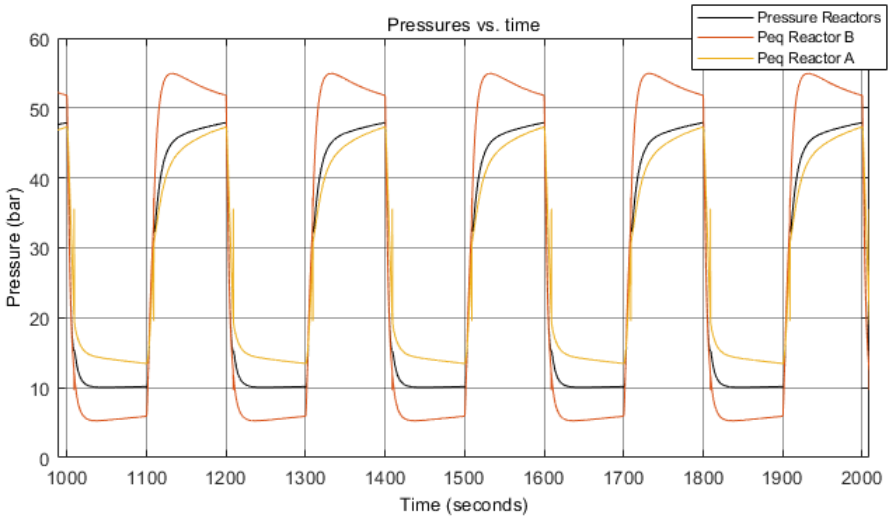


[h]

Figure 17: Evolution of pressure (bar) vs. time (s), where the pressure of reactor B is displayed. The pressure difference between the reactors is small and therefore only one pressure curve has been shown.

equilibrium pressure in this model is higher because of a higher temperature in the reactor beds, as was also noticed by Paýa et al. [10]. The reason for a higher bed temperature can be caused by a smaller amount of exchanged hydrogen, also causing a higher average hydrogen concentration in the MHs, which will further increase the equilibrium pressure. Another factor that increases the pressures, is the absence of a factor decreasing the equilibrium pressures when an MH alloy is near the $\alpha$-region, or increasing the equilibrium pressures near the $\beta$-region [11]. The pressure difference between the two reactors during the simulation is small ($\approx 0.25$ bar), and therefore only the pressure of reactor B has been shown.

The temperature of both the reactors and temperature of the HTF outlets are plotted in figure 19. It is clear that the model accurately predicts the HTF temperature at the outlet at reactor A. The temperature rise during the regeneration half cycle at reactor B is faster than observed in figure 20. The temperature decrease at reactor B, during the cooling half cycle, is faster too, which may indicate that the overall heat transfer coefficient between the reactors and the HTF circuit is higher than at the model of Paýa.
The model of Paýa tends to over predict the performance somewhat, resulting in a larger temperature decrease than observed in his experiments [11]. The model, presented in this thesis, over predicts the performance at the

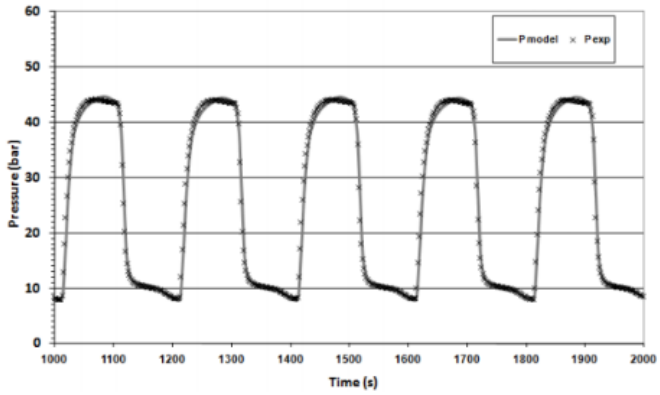


[h]

Figure 18: Evolution of pressure (bar) vs. time (s), where the pressure of reactor B is displayed. Data obtained by Paya et al. [10]

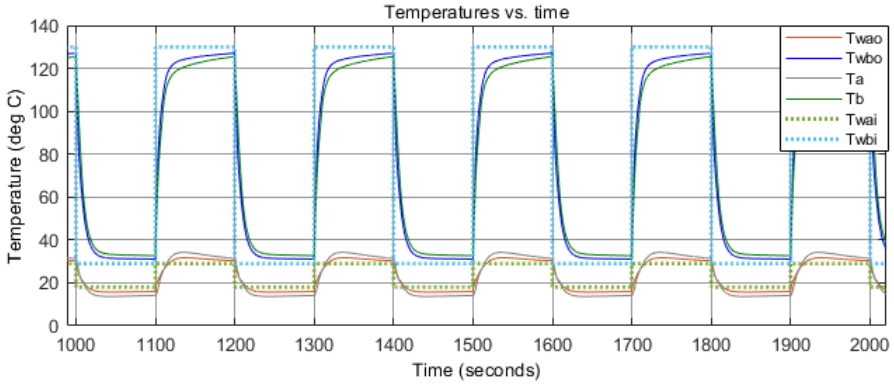


Offset=0

Figure 19: Evolution of temperatures ($°C$) vs. time (s), where $T_{wAi}/T_{wBi}$ and $T_{wAo}/T_{wBo}$ are the HTF inlet/outlet temperatures and $T_a/T_b$ are the reactor temperatures obtained by the model.

last 20 s of the cooling half cycle, as was also noticed by Paya et al. [10]. This is caused by an over prediction of desorbed hydrogen, see figures 22, 23 and 24. The HTF temperature, at reactor A during the cooling half cycle, predicted by the model is around $15°C$, achieving a $\Delta T = 3°C$, giving an average cooling capacity of 598 W during the cooling half cycle. During this half cycle absorbing reactor B is cooled down to $29°C$. Figure 21 shows the temperatures in reactor A in a more detailed manner.

Figure 22 indicates the hydrogen mass flow between the reactors in standard litres per minute, SL/min (Paýa et al. [10] and Paýa [11] use that unit to measure the hydrogen mass flow). The model shows a very similar hydrogen mass flow, compared with the results Paýa et al. obtained in their article [10], see figures 23 and 24. The total amount of hydrogen exchanged in this model is similar, compared with the experimental results from Paýa. The peaks in hydrogen mass flow observed in the model are high, which may be due to a different

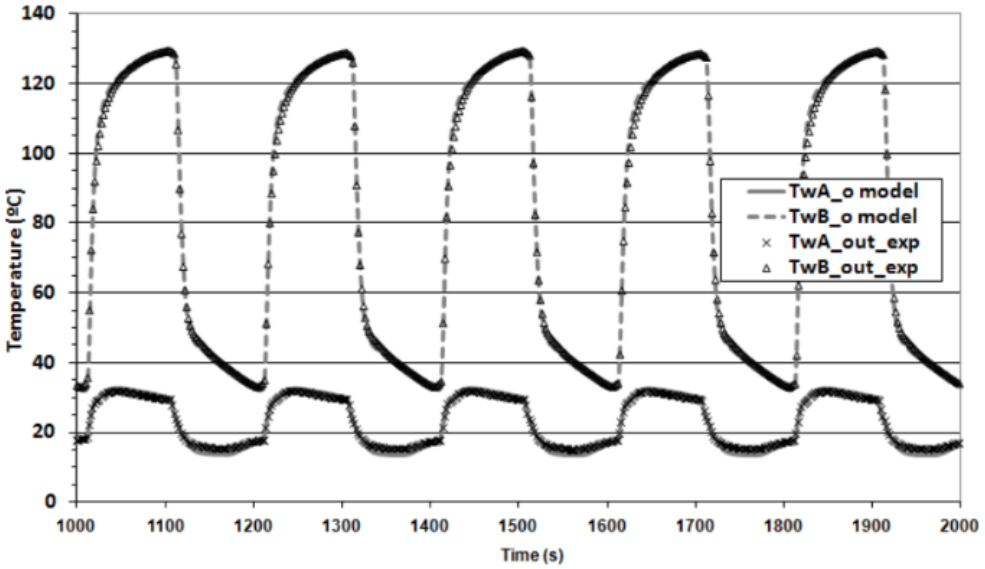


Figure 20: Evolution of temperatures ($°C$) vs. time (s). Data obtained by Paýa [11]

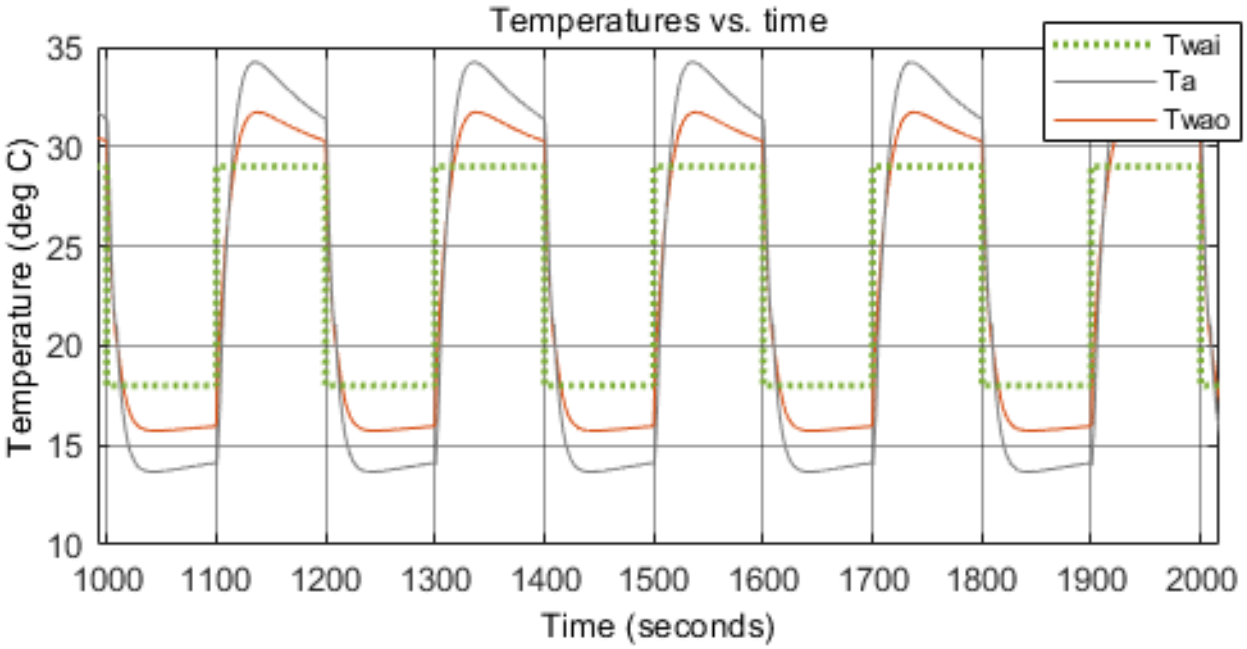


Figure 21: Evolution of temperatures ($°C$) vs. time (s), where $T_{wAo}/T_{wAi}$ are the HTF outlet/inlet temperatures and $T_a$ is the reactor temperature obtained by the model.

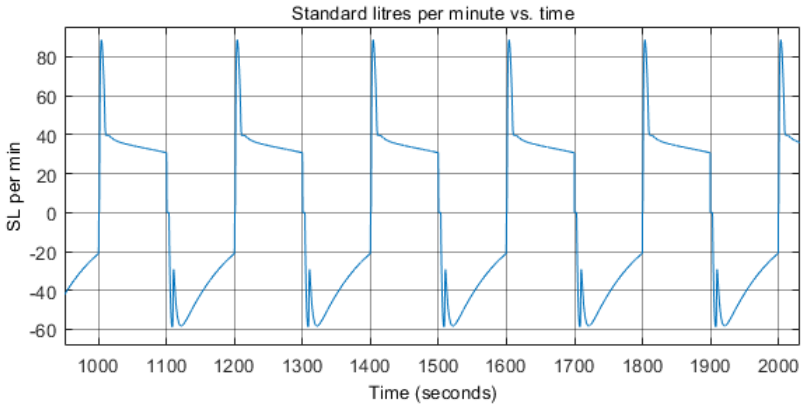


Figure 22: Evolution of hydrogen mass flow (SL/min) vs. time (s), where a positive number indicates a hydrogen flow from reactor A to B, and vice versa.

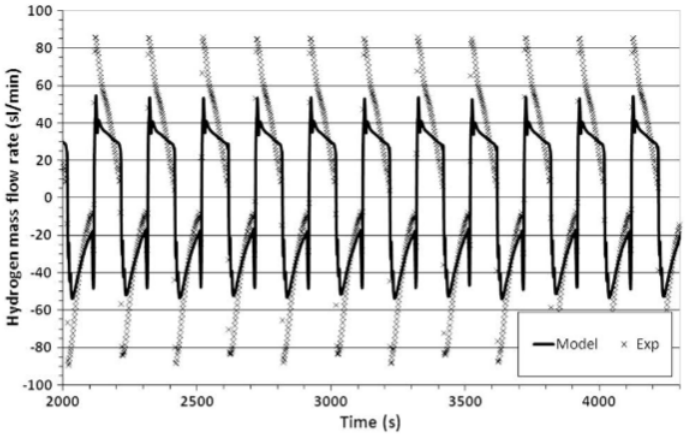


Figure 23: Evolution of hydrogen mass flow (SL/min) vs. time (s) from the model by Paýa et al. [10], where a positive number indicates a hydrogen flow from reactor A to B, and vice versa.

implementation in the transition period as the peaks occur during that time. For clarity, the hydrogen mass flow in kilograms per second has been given in figure 25.

The hydrogen concentration in reactor A and B are shown in figure 26. The cooling capacity of the system is shown in figure 27. As a consequence of the over prediction of exchanged hydrogen near the end of the cooling cycle, the cooling capacity will be over predicted as well. It should be noted that during the transition phase a peak occurs in the cooling capacity, which is a consequence of the change of temperature of the in-flowing HTF, while the reactor is still cold or hot. In figure 27, this peak has been left out for clarity, as it does not represent 'useful' cooling capacity.

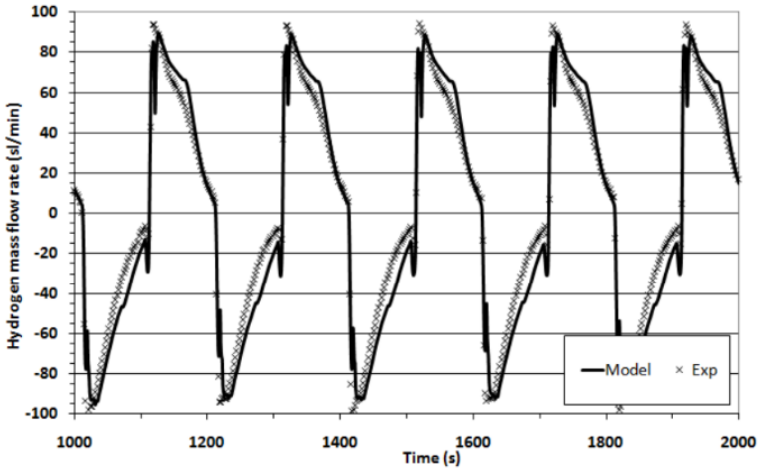


Figure 24: Evolution of hydrogen mass flow (SL/min) vs. time (s) from the model by Paýa [11], where a positive number indicates a hydrogen flow from reactor A to B, and vice versa.

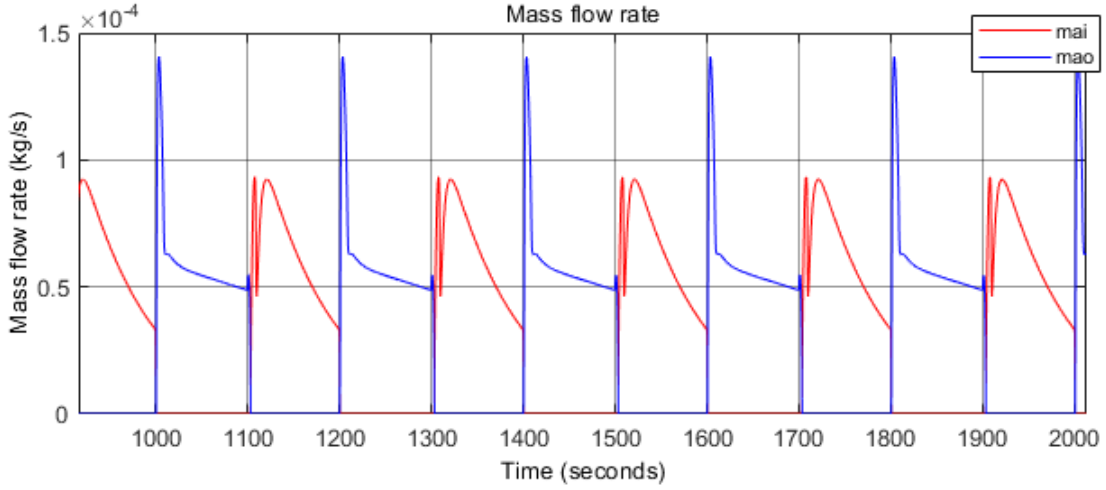


Figure 25: Evolution of hydrogen mass flow (kg/s) vs, time (s). mai and mao represent respectively the massflow in and out of reactor A. Note that when mai is zero, mao is non zero and vice versa.

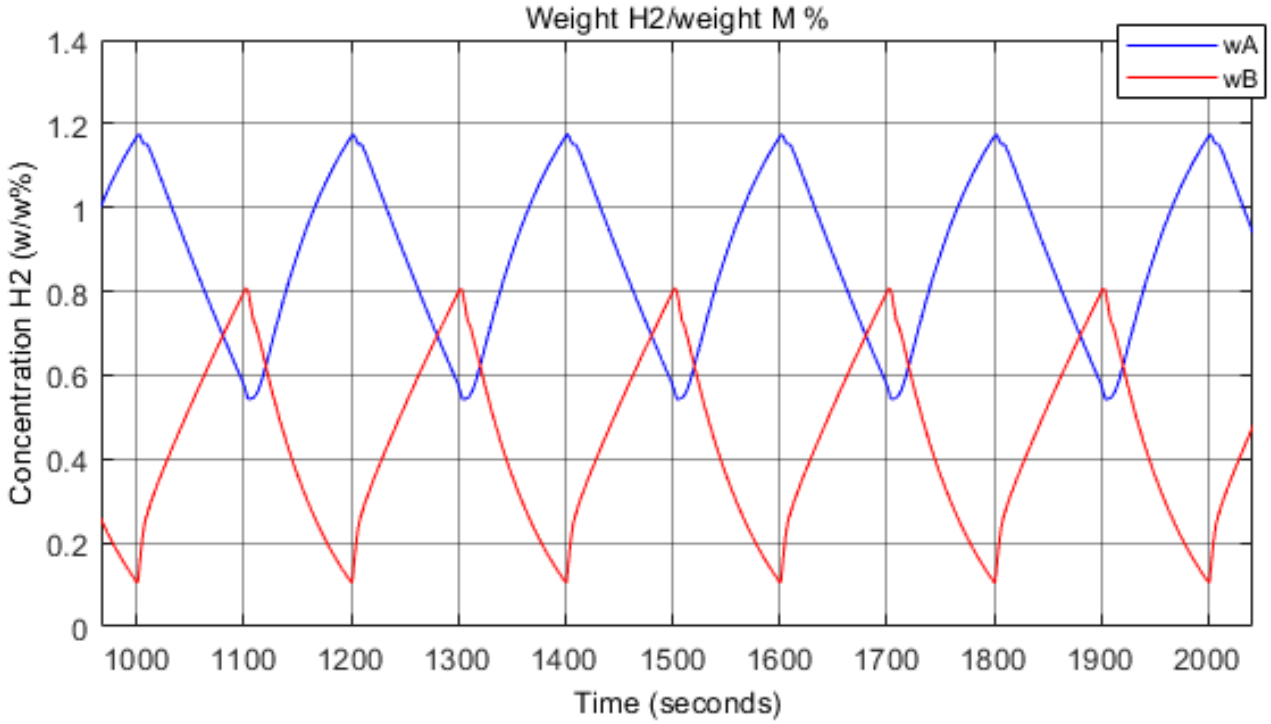


Figure 26: Evolution of hydrogen concentration (w/w%) in reactors A and B vs. time (s).

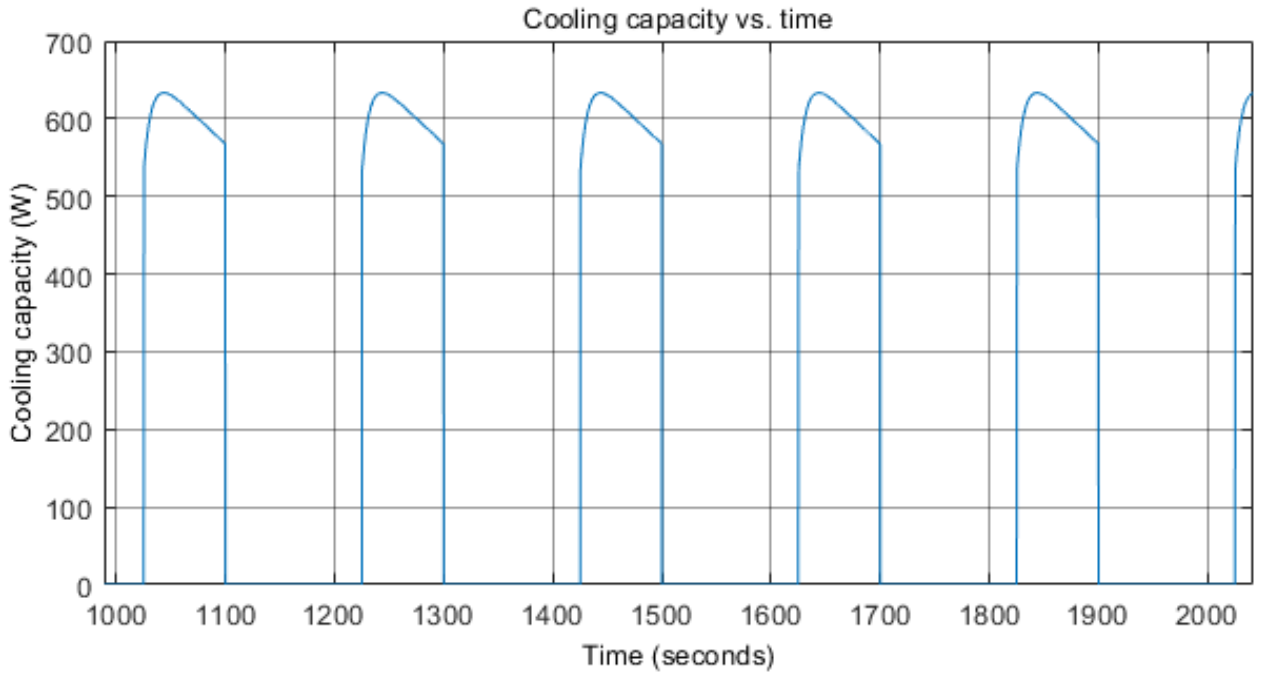


Figure 27: Cooling capacity (W) in reactors A and B vs. time (s)

## 6.3 Conclusion of validation

The overall system performance prediction is similar to the results Paýa obtained during his simulations and experiments [10, 11]. The reactor geometries, some initial conditions and system parameters are not clarified by Paýa and therefore realistic values for these parameters have been chosen. These parameters can easily be adjusted to an experimental setup. The transition period is not identically implemented, causing a higher peak in hydrogen mass flow and temperature change. Also, the PCT-characteristics implemented into the model are implemented in a simpler manner, comparing with Paýa, which causes the model to behave slightly different.

# 7 Results of the low temperature MHCS simulation and discussion

As was described in chapter 4, the MH alloy,$Ti_{0.95}Zr_{0.05}Cr_{1.2}Mn_{0.8}$ is introduced to the model, with the objective of obtaining lower feasible cooling temperatures, while maintaining cooling capacity. There has been done very little research on the feasibility of low temperature MH refrigeration systems in the last couple of years [19, 21], and no research with capillary tube bundle reactors or plate reactors. In this chapter, the performance of the new system will be analyzed and discussed.

Seawater will be used to cool or heat the reactors to $T_m = 20°C$. The system needs to produce useful cold at $T_c = -20 - -10°C$, to be used in an ice slurry machine. The hot temperature $T_h$ influence, generated by exhaust gases, will be analyzed by means of a sensitivity analysis. Table 11 show the parameters of the metal hydrides and their values. Note that the values of the kinetic constant K are equal to that of metal hydride $Ti_{0.99}Zr_{0.01}V_{0.43}Fe_{0.09}Cr_{0.05}Mn_{1.5}$, caused by the lack of precise data of this and other low temperature MH alloys. The desorption reaction activation energy has been taken at a lower value, compared with the first low temperature MH, and is based on other titanium based MH alloys [9]. A higher value for the reaction activation energy will cause a decrease in hydrogen absorption/desorption, see equation 6, and vice versa. The reaction activation energy is difficult to measure in experiments [11].

Table 11: Metal hydride parameters and their corresponding values.

| Parameter | Value |
|---|---|
| $K_{A,abs}$ | $3 \cdot 10^8$ |
| $K_{A,des}$ | $9 \cdot 10^4$ |
| $K_{B,abs}$ | $1.52 \cdot 10^5$ |
| $K_{B,des}$ | 294 |
| $E_{A,abs}$ | $35000 J/mol$ |
| $E_{A,des}$ | $43000 J/mol$ |
| $E_{B,abs}$ | $43651 J/mol$ |
| $E_{B,des}$ | $28976 J/mol$ |

## 7.1 Influence of cooling temperature on cooling capacity

The cooling temperature has influence on a refrigeration system, i.e. a lower cooling temperature results in a lower cooling capacity. This is a consequence of a decrease in reaction kinetics and a subsequent decrease in exchanged hydrogen. The HTF massflow, cooling and regeneration cycle times and other parameters not involved in the kinetic equation (equation 6) are identical to the values presented in chapter 6. Figure 28 shows the respective cooling capacity plotted for one cooling cycle. Some time is needed for the system to be able to generate useful cold, due to a temperature difference between the reactor and HTF when the cooling cycle starts. Reactor A will be at temperature $T_m$ at the start of the cooling cycle, while the in-flowing HTF is at $T_c$, causing a negative peak in cooling capacity (as mentioned in chapter 6). The opposite occurs at the start of the regeneration cycle, when the reactor will be colder than the in-flowing HTF. These peaks are left out of the figures showing the cooling capacity, as those peaks do not represent useful cooling capacity. The MHCS needs more time to cool down, as the in-flowing HTF temperature decreases. Therefore lower operating temperatures do not only decrease the maximum cooling capacity, but also the total time useful cold is generated, further

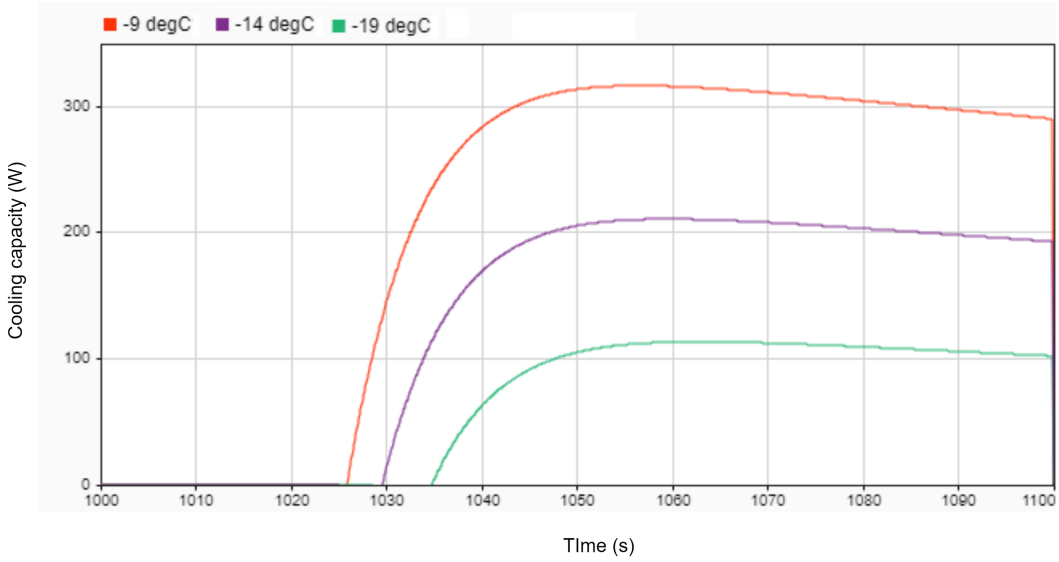


Figure 28: Cooling capacity (W) in reactor A vs. time (s). The referred temperatures are the temperatures of the HTF flowing into reactor A. $T_h = 150°C$.

decreasing the average cooling capacity. Figure 28 clearly shows the mentioned decline in cooling capacity with decreasing temperatures.

To further indicate the cooling temperature on the MHCSs performance, the mean COP and the mean cooling capacity are shown in figure 29. It can be seen in this figure that the mean cooling capacity and the mean COP decrease with a lower cooling temperature, as should be expected from the system. A higher desorption temperature will increase the desorption reaction rate and thus increase the performance of the system. An increase of the bed temperature in reactor A during the cooling phase will increase the equilibrium pressure of the low temperature MH. This has as a consequence that the difference in pressures increases and more hydrogen will be exchanged between the reactors.

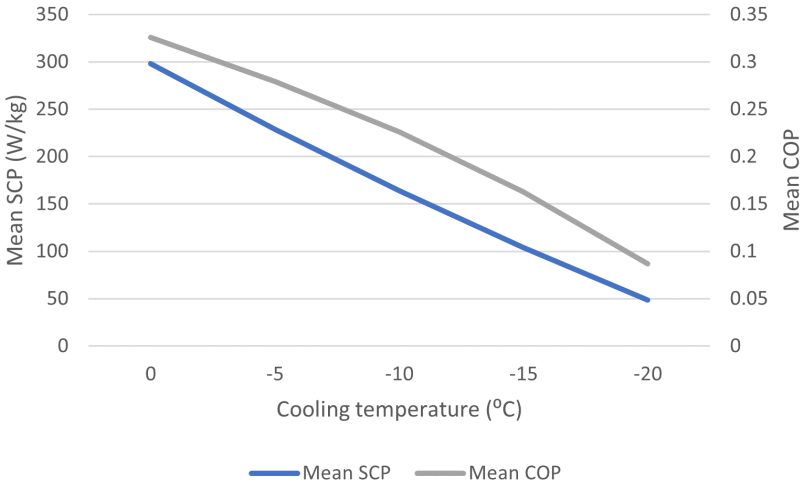


Figure 29: Mean SCP (W/kg) and mean COP vs. cooling temperature ($°C$). The referred temperatures are the respective cooling temperatures. Driving temperature $T_h$ (high temperature HTF flowing into reactor B) is set at $150°C$.

## 7.2 Influence of driving temperature on cooling capacity

The driving temperature $T_h$ has an influence on the system performance, just as the cooling temperature has. To investigate the system performance at different driving temperatures, the model has been run with $T_h$ between $130 - 170°C$. The cooling temperature $T_c$ is set at $-9°C$. As can be seen in figure 30, the driving temperature heavily influences the performance of the MHCS. The increase in pressure, due to higher temperatures, and with that an increase in pressure difference causes an increase in hydrogen mass flow between the reactors. Because of this, it is preferred to have the driving temperature as high as the system allows. It is, however, not possible to increase the driving temperature indefinitely as a consequence of the critical temperature of MHs and the increase in pressure during the regeneration cycle. The pressure of reactor A is displayed in figure 31.

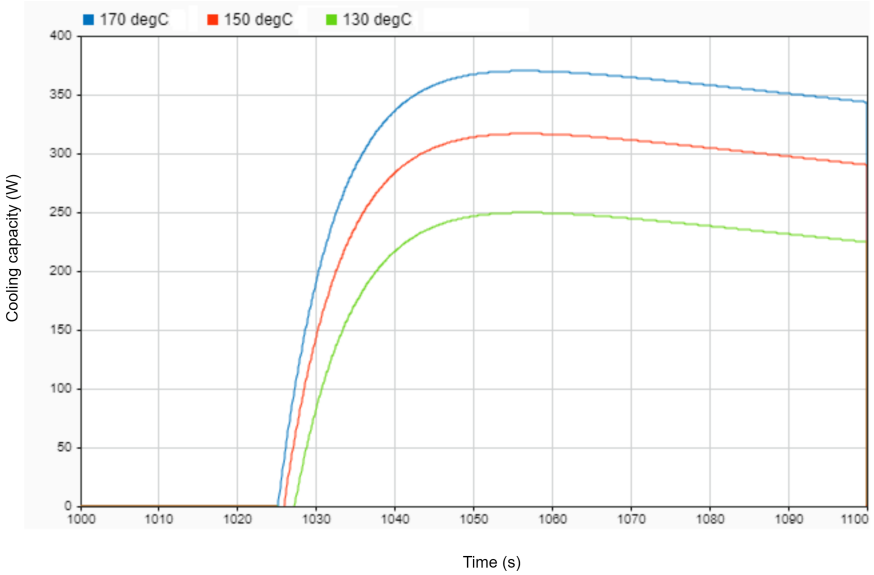


Figure 30: Cooling capacity (W) in reactor A vs. time (s). The referred temperatures are the respective driving temperatures. Cooling temperature $T_c$ (low temperature HTF flowing into reactor A) is set at $-9°C$.

As mentioned before, the pressure difference between both reactors is relatively small and therefore only the pressure of reactor A is shown. As can be seen in the figure, the pressure during the regeneration cycle increases with a higher driving temperature. It is expected from the PCT-characteristics that there is a larger pressure increase occurring from 150 to 170 $°C$, than from 130 to 150 $°C$. The mean cooling capacity $Q_c$ and mean COP are shown in figure 32. It can be seen that the COP increases with a higher driving temperature until approximately 155 $°C$. The low temperature MH will hardly regenerate at driving temperatures lower than 130 $°C$. As in this model the PCT-characteristics have been chosen to be fairly simple, the equilibrium pressure of the low temperature MH will in reality be lower and the equilibrium pressure of the high temperature MH higher (near the borders of the $\alpha/\beta$-regions), causing an experimental MHCS with a low driving temperature to perform even worse than this model shows.

Another beneficial effect of a higher driving temperature is the ability to decrease the regeneration cycle time, making the cooling cycle a relatively larger part of the systems operation cycle and thus further increasing the average cooling capacity.

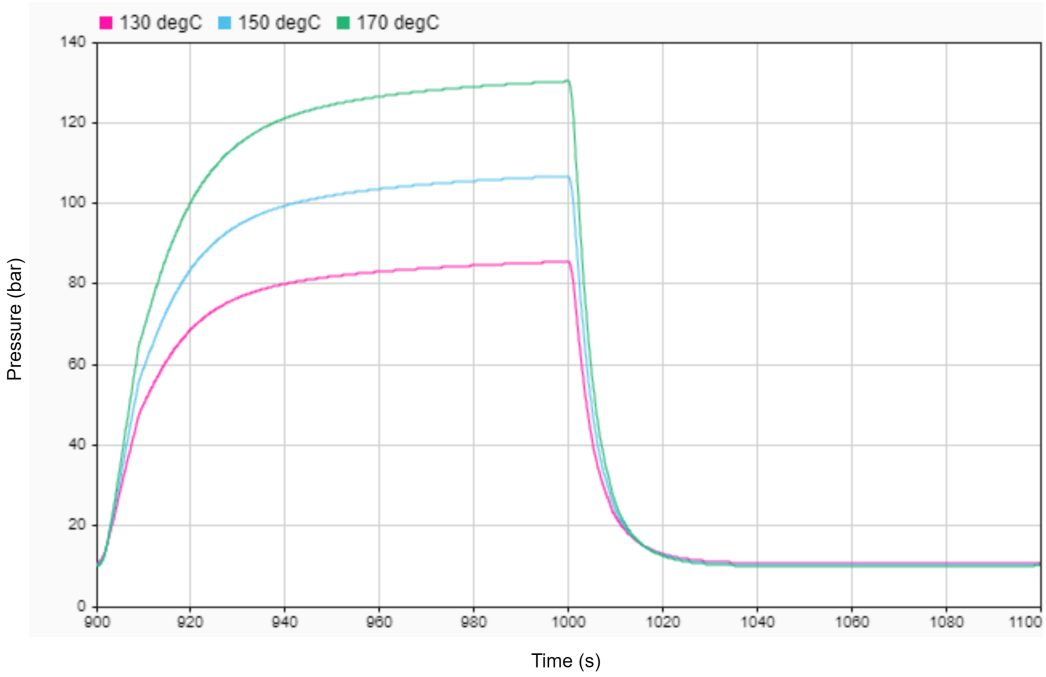


Figure 31: Pressure (bar) in reactor A vs. time (s). The referred temperatures are the respective driving temperatures. Cooling temperature $T_c$ (low temperature HTF flowing into reactor A) is set at $-9°C$.

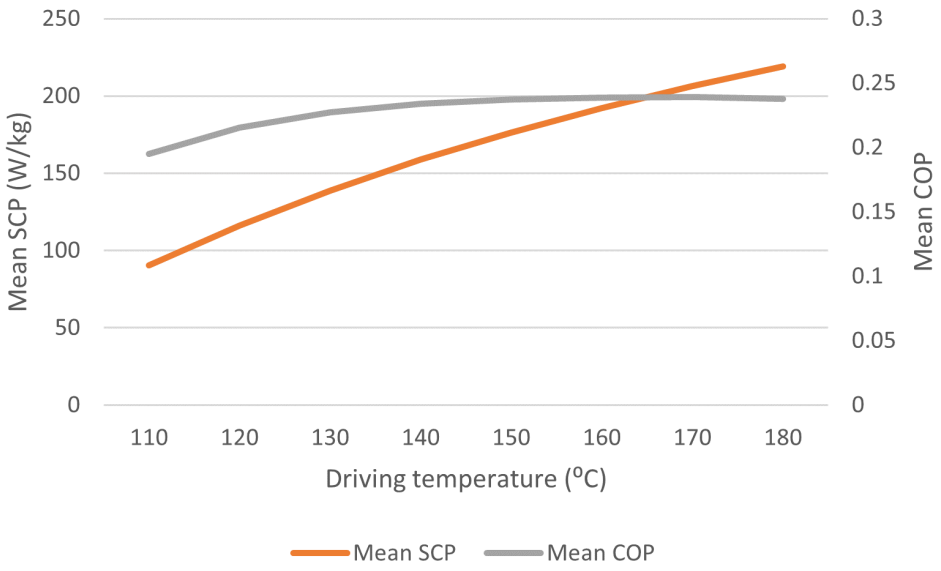


Figure 32: Mean SCP (W/kg) and mean COP vs. driving temperature ($°C$). The referred temperatures are the respective driving temperatures. Cooling temperature $T_c$ (low temperature HTF flowing into reactor A) is set at $-9°C$.

## 7.3 Influence of desorption reaction rate constant K on SCP

Reaction rate constant K directly influences the absorbed and desorbed hydrogen in the reactors. Equation 6 shows a linear relation between the exchanged hydrogen and reaction rate constants $K_{abs}$ and $K_{des}$. The reaction rate constants for the new low temperature MH, introduced in this chapter, is not known, and thus

simulations have been performed to measure the influence of the desorption reaction rate constant on the system performance. In the previous subsections of this chapter, the reaction rate constant was assumed to be equal to the value of the constant of the low temperature MH in chapter 6 ($K = 9 \cdot 10^4$). Figure 33 shows the relation between reaction rate constant $K_{des}$ and the mean SCP. It can be seen that an increase of $K_{des}$ will increase the performance of the system, as expected from equation 6. After a value of $K = 10^5$, a further increase only slightly increases the system performance. The relation between the mean COP and the reaction rate constant

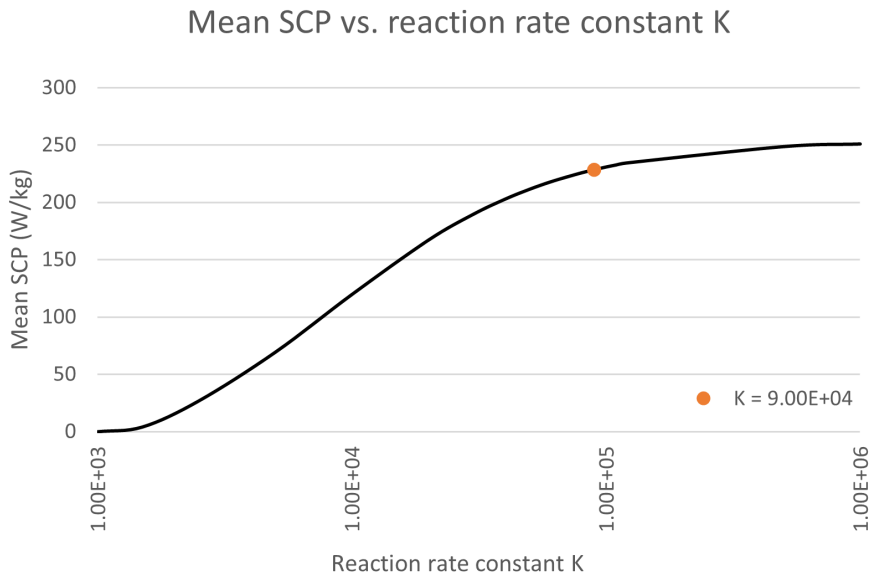


Figure 33: Mean specific cooling power (W/kg) and mean COP vs. reaction rate constant $K_{des}$. Cooling temperature $T_c$ (low temperature HTF flowing into reactor A) is set at $-9°C$. Driving temperature is set at $150°C$.

is shown in figure 34. By increasing the intrinsic reaction kinetics, by increasing the reaction rate constant, a maximum mean COP of 0.3 seems to be achievable with a driving temperature of 150 °C. This implies that a COP higher than 0.3 may be possible the achieve with an optimized system.

## 7.4 Scaling up to a 16 kW system

The research and presented simulation in this thesis suggest that MHCSs could be interesting and technically feasible in the application of a low temperature ice slurry cooling system that makes use of exhaust gases of the fishing vessel. This because an SCP of 75-100 W/kg MH for a four reactor system seems to be realistically achievable. For a 16-kW system, this means that 160 to 213 kg of total MH alloy mass will be needed. The total filled reactor mass for a system of capillary tube bundle reactors will be 515 to 686 kg, assuming the same weight over weight ratio as Paýa [11]. This results in an SCP of 23.3-31.1 W/kg, excluding the weight of the HTF network. This may be further reduced by implementing the plate reactor presented by Weckerle et al. [23]. The plate reactor system is better scalable than the capillary tube bundle reactor system and will have relatively less parasitic metallic mass in the system. The plate reactor system will also have a smaller pressure drop, as the average distance hydrogen needs to travel is smaller.

A conventional ice slurry system, the Recom Ice Systems 15 kW SL100, has a total system SCP of around 11.5

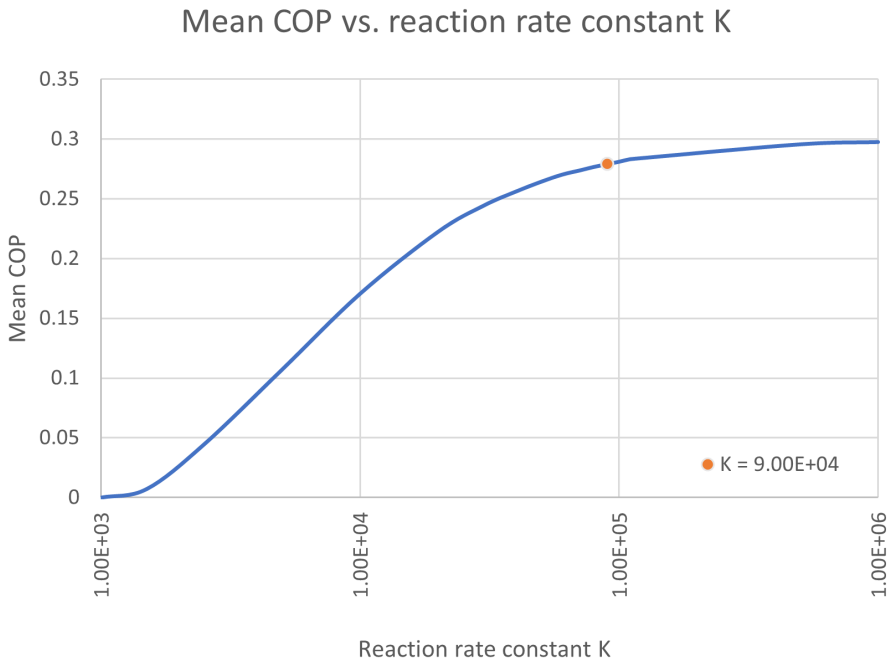


Figure 34: Mean COP vs. reaction rate constant $K_{des}$. Cooling temperature $T_c$ (low temperature HTF flowing into reactor A) is set at $-9°C$. Driving temperature is set at $150°C$.

W/kg, which seems achievable for a MHCS as well. This indicates that the implementation of a low temperature MH based ice slurry refrigerator may be possible in fishing vessels.

## 7.5 Further discussion

The previous chapter found that the driving temperature, cooling temperature and reaction rate constant $K_{des}$ all heavily influence the performance of the MHCS. A decrease in cooling temperature negatively impact the cooling capacity. An increase in driving temperature increases the cooling capacity, but the temperature can only be increased to a certain extend. If the reaction rate constant $K_{des}$ is increased the cooling capacity will increase.

The influence of the cooling temperature was already mentioned in many other studies about MHCS [8, 10, 11, 18, 19]. As the exact influence of the cooling temperature on this particular low temperature MH and reactor geometry has not been researched, it has been done in this thesis. This study found that a mean cooling capacity of around 370 W and a mean COP of 0.22 is obtainable for this MHCS ($T_c = -9°C, T_h = 170°C$). This indicates that a maximum mean sytem SCP of 31 W/kg is possible to achieve for a four reactor system, excluding the weight of the HTF network. Comparing the SCP with that of a conventional 15 kW ice slurry refrigerator (total system SCP of 11.5 W/kg) this seems reasonable. Comparing the performance obtained from the simulations with the experimental performance of Imoto et al.[19], see tabel 4, this MHCS performs better in terms of SCP. The COP of Imoto et al. [19] is higher, but it is unclear if this referres to the maximum or mean COP in their research. Also, the heat supply in the flyshooter fishing ships is abundant due to the large diesel engine, thus it can be argued that the COP is a less important system characteristic than SCP.

MHCS also have a high volumetric cooling power, creating a relatively large cooling effect while being small in size [11]. A total reactor volume of 2.8 litres (4 reactors of 0.7 litres) will be capable of generating 370 W of cooling effect at around -10 °C, as was shown in this study.
The fishing vessels on Goeree-Overflakkee may be a suitable location for such a system, as they are in need of sustainable ice slurry refrigerator and the MHCS shows .

### 7.5.1 Limitations

The plate reactor presented by Weckerle et al. [23] is easily scalable, compared with a capillary tube bundle reactor. Increasing the size of a capillary tube bundle reactor will greatly decrease the system performance, because of an increase in pressure drop over the reactor bed. The quantity of this pressure drop was not studied in this thesis, as the numerical model is 0 D.

Most of the results obtained in this research are done with a reaction rate constant of $K = 9 \cdot 10^4$. Decreasing the reaction rate constant will decrease the cooling capacity. For many low temperature MHs, including $Ti_{0.95}Zr_{0.05}Cr_{1.2}Mn_{0.8}$, this reaction rate constant is not known. Thus, the reaction rate constant $K_{des}$ is a limitation to the reliability of the simulation results.

Another limitation is the usage of the NTU method in the model. The model calculates the heat flow between the water circuit and the metallic tube and the heat flow between the metallic tube and MH bed. The NTU method is used to calculate the effectiveness of a heat exchanger between two fluids, but in this thesis it is used between the metallic tube and a fluid, where the metallic tube is seen as a saturated liquid with a uniform but changing temperature. The MH bed and the metallic tubes have a uniform temperature, thus the NTU method is not used on that side.

The HTFs are assumed to have the same heat capacity and density as water. As water will not be used in the MHCS, due to the high and low temperatures, other HTFs should be considered.

# 8 Conclusions

The main research question this thesis aimed to answer was whether it is technically feasible to generate a cooling effect of 16 kW at -10 to -20 °C on a diesel-powered fish vessel with a metal hydride cooling system. This to understand whether this technique could be employed in lowering the $CO_2$ emissions of fishing vessels specifically in Goeree-Overflakkee as a pilot case.

In this thesis, the working principle and limitations of MHCSs were described. The development of a numerical model was investigated and a numerical model was developed. The numerical model has been validated by using a numerical model and experimental data [10, 11].

By simulating the MHCS, the thesis was able to simulate the system performance under different operating conditions. One of the findings of this simulation was that the cooling and driving temperature in a low temperature MHCS heavily influence the system performance, which means the operating conditions are highly important to ensure proper functioning. It was found that an increase in driving temperature increases the system performance. A maximum mean COP of 0.24 is reached at $T_h = 170°C$ and $T_c = -9°C$, but decreases if the driving temperature increases further. The maximum obtainable mean SCP of the system, by changing the driving temperature, is 206 W/kg at $T_h = 170°C$ and $T_c = -9°C$. A further driving temperature increase results in undesirably large gas pressures. A decrease in cooling temperature decreases the performance of the system. A total system SCP, excluding the HTF network, of 31 W/kg is possible, based on the simulations.

The desorption reaction rate constant $K_{des}$ directly influences the hydrogen mass flow and therefore influence the system performance as well. When the desorption reaction rate constant is smaller than $10^4$ the performance quickly decreases. If the constant is larger than $10^5$ the increase in performance will be negligible. By increasing the constant, a maximum mean COP of 0.3 may be reached ($T_c = -9°C, T_h = 150°C$).

In conclusion, the implementation of a MHCS as a low temperature ice slurry cooling system is technically feasible, despite some limitations to its performance and efficiency. This suggests an exciting opportunity for its application in the challenge of lowering the $CO_2$ emissions of the fishing fleet of Goeree-Overflakkee specifically, but also in different fishing fleets around the world if the H2GO pilot proves to be successful.

# 9 Recommendations

There are a few recommendations to this study that could be addressed in future research. First, while the outcomes of this thesis research suggest that the implementation of MHCS as a low temperature ice slurry cooling system is feasible, further, preferably experimental, research should be conducted to further investigate the possibilities and limitations of low temperature MHCS.

The pressure drop, temperature gradients in the MH powder and metallic tubes may influence the system in a negative way. As an example, in this thesis the NTU method is used to account for a temperature gradient in the HTF. A spatial model will remove the need of such assumptions.

Moreover, it is of great importance to accurately simulate the intrinsic reaction kinetics in the MHCS. It is very difficult to measure the sorption curves of a fast-reacting MH and the experimental field needs further improvement to simulate a low temperature MHCS more accurately. In a coupled reactor system, such as described in this thesis, the mass flow of hydrogen derives from the reaction kinetics of both reactors. Hence, it is difficult to simulate the amount of exchanged hydrogen precisely, unless the reaction kinetics and heat flow of all the reactors present in the system are modelled properly. This thesis has provided an overall good prediction of the hydrogen mass flow rate. To further improve the prediction of the model, however, the PCT-characteristics could be modelled in a more complex manner near the plateau region boundaries.

Another aspect that should be considered for future research is that for a numerical model of an MHCS to perform as accurately as possible, it is important to model the PCT-characteristics of the MH alloys present in the system as accurately as possible. This model predicts the equilibrium pressures accurately between approximately 0.5-1.5 w/w% hydrogen concentration in the MH's. Outside of these concentrations, another factor compensating for the decrease in equilibrium pressure in the $\alpha$-region and increase in equilibrium pressure in the -region should be implemented to further increase the accuracy of the MHCS model.

The implementation of gradual variations of metal hydride alloy properties when switching between half cycles were part of the simulation developed in this thesis. This aspect of dynamic models is often neglected, making many numerical models less robust than the model presented in this thesis. Future research should further enhance the implementation of the transition period, f.e. including the equilibrium pressures.

The implementation of different temperature levels could be researched in future work as well. This model switches to the cold HTF network, while reactor A is still at the ambient temperature. A separate temperature level between the ambient and cold temperatures, as well as a switch in the hydrogen connection tube, may be a useful step to implement, as it will decrease the sensible heat losses.

Finally, the influence of other system and MH parameters, such as the activation energy and the metallic mass, can be measured by simulations in the model. By performing those simulations, more knowledge about increasing the performance of MHCSs can be obtained.

# References


[1] A. Arteconi and F. Polonara. "Demand side management in refrigeration applications". In: *International Journal of Heat and Technology* 35.1 (2017), pp. 58–63.

[2] S. A. Kalogirou. "Chapter 6- Solar Space Heating and Cooling". In: *Solar Energy Engineering (Second Edition), Academic Press, Boston* (2014), pp. 323–395.

[3] P. Muthukumar, A. Kumar, N. N. Raju, K. Malleswararao, and M. M. Rahman. "A critical review on design aspects and developmental status of metal hydride based thermal machines". In: *international journal of hydrogen energy* 43.37 (2018), pp. 17753–17779.

[4] P. Muthukumar, M. Maiya, and S. Murthy. "Experiments on a metal hydride-based hydrogen storage device". In: *International Journal of Hydrogen Energy* 30.15 (2005), pp. 1569–1581.

[5] P. Muthukumar and M. Groll. "Erratum to "Metal hydride based heating and cooling systems: a review"[International Journal of Hydrogen Energy (2010) 35: 3817–3831]". In: *international journal of hydrogen energy* 35.16 (2010), pp. 8816–8829.

[6] M. Martin, C. Gommel, C. Borkhart, and E. Fromm. "Absorption and desorption kinetics of hydrogen storage alloys". In: *Journal of Alloys and Compounds* 238.1-2 (1996), pp. 193–201.

[7] M. Linder. "Automotive cooling systems based on metal hydrides". In: (2010).

[8] A. Satheesh. "Thermal modeling and performance investigations of metal hydride based heat pumps". PhD thesis. 2010.

[9] T. Voskuilen, E. Waters, and T. Pourpoint. "A comprehensive approach for alloy selection in metal hydride thermal systems". In: *International journal of hydrogen energy* 39.25 (2014), pp. 13240–13254.

[10] J. Paya, M. Linder, E. Laurien, and J. Corberan. "Dynamic model and experimental results of a thermally driven metal hydride cooling system". In: *International journal of hydrogen energy* 34.7 (2009), pp. 3173–3184.

[11] J. Payá Herrero. "Modelling and analysis of a metal hydride cooling system". PhD thesis. Universitat Politècnica de València, 2010.

[12] F. Yang, X. Meng, Z. Zhang, and Y. Yu. "Selection of alloys in a metal hydride heat pump–a new procedure". In: *Proceedings of international refrigeration and air conditioning conference at Purdue, West Lafayette, USA*. 2008.

[13] G. Sandrock and G. Thomas. "The IEA/DOE/SNL on-line hydride databases". In: *Applied Physics A* 72.2 (2001), pp. 153–155.

[14] R. Van Hal, O. G. Bos, and R. G. Jak. *Noordzee: systeemdynamiek, klimaatverandering, natuurtypen en benthos: achtergronddocument bij Natuurverkenning 2011*. Tech. rep. Wettelijke Onderzoekstaken Natuur & Milieu, 2011.

[15] U. S. N. R. Commission. "0420 - E111 - Emergency Diesel Generators - Chapter 06 - Engine Cooling Systems". 2011.

[16] D. P. Nolan. *Fire Pump Arrangements at Industrial Facilities*. Gulf Professional Publishing, 2017.

[17] M. Ron. "A hydrogen heat pump as a bus air conditioner". In: *Journal of the Less Common Metals* 104.2 (1984), pp. 259–278.

[18] P. Golben and E. Huston. *Design and fabricate a metallic hydride heat pump with a cooling capacity of 9000 Btu/h*. Tech. rep. ERGENICS INC WYCKOFF NJ, 1989.

[19] T. Imoto, T. Yonesaki, S. Fujitani, I. Yonezu, N. Hiro, K. Nasako, and T. Saito. "Development of an F-class refrigeration system using hydrogen-absorbing alloys". In: *International journal of hydrogen energy* 21.6 (1996), pp. 451–455.

[20] M. Gopal and S. Murthy. "Experiments on a metal hydride cooling system working with ZrMnFe/MmNi4. 5Al0. 5 pair". In: *International journal of refrigeration* 22.2 (1999), pp. 137–149.

[21] F. Qin, J. Chen, M. Lu, Z. Chen, Y. Zhou, and K. Yang. "Development of a metal hydride refrigeration system as an exhaust gas-driven automobile air conditioner". In: *Renewable energy* 32.12 (2007), pp. 2034–2052.

[22] M. Linder, R. Mertz, and E. Laurien. "Experimental results of a compact thermally driven cooling system based on metal hydrides". In: *International Journal of Hydrogen Energy* 35.14 (2010), pp. 7623–7632.

[23] C. Weckerle, I. Bürger, and M. Linder. "Novel reactor design for metal hydride cooling systems". In: *International Journal of Hydrogen Energy* 42.12 (2017), pp. 8063–8074.

[24] R. Hegner, H. Dittus, Schier, H. Friedrich, C. Weckerle, and I. Bürger. "Thermomanagement and cabin climatization in electric vehicles using a hydrogen based A/C-unit". In: *2019 Fourteenth International Conference on Ecological Vehicles and Renewable Energies (EVER)*. IEEE. 2019, pp. 1–7.

[25] C. Weckerle, M. Dörr, M. Linder, and I. Bürger. "A Compact Thermally Driven Cooling System Based on Metal Hydrides". In: *Energies* 13.10 (2020a), p. 2482.

[26] C. Weckerle, M. Nasri, R. Hegner, I. Bürger, and M. Linder. "A metal hydride air-conditioning system for fuel cell vehicles–Functional demonstration". In: *Applied Energy* 259 (2020b), p. 114187.

[27] S. Mohammadshahi, E. M. Gray, and C. Webb. "A review of mathematical modelling of metal-hydride systems for hydrogen storage applications". In: *international journal of hydrogen energy* 41.5 (2016), pp. 3470–3484.

[28] J. Payá, M. Linder, R. Mertz, and J. Corberán. "Analysis and optimization of a metal hydride cooling system". In: *International Journal of Hydrogen Energy* 36.1 (2011), pp. 920–930.

[29] T. Nishizaki, K. Miyamoto, and K. Yoshida. "Coefficients of performance of hydride heat pumps". In: *Journal of the Less Common Metals* 89.2 (1983), pp. 559–566.

[30] S. Mellouli, F. Askri, H. Dhaou, A. Jemni, and S. Nasrallah. "Parametric studies on a metal-hydride cooling system". In: *international journal of hydrogen energy* 34.9 (2009), pp. 3945–3952.

[31] V. Sharma, E. Kumar, and S. Murthy. "Influence of dynamic operating conditions on the performance of metal hydride based solid sorption cooling systems". In: *International Journal of Hydrogen Energy* 40.2 (2015), pp. 1108–1115.

[32] C. Weckerle, I. Bürger, and M. Linder. "Numerical optimization of a plate reactor for a metal hydride cooling system". In: *Submitted to International Journal of Hydrogen Energy* (2019).

[33] A. Satheesh and P. Muthukumar. "Performance investigations of a single-stage metal hydride heat pump". In: *International journal of hydrogen energy* 35.13 (2010), pp. 6950–6958.

[34] J. Vanhanen, M. Hagström, and P. Lund. "Combined hydrogen compressing and heat transforming through metal hydrides". In: *International journal of hydrogen energy* 24.5 (1999), pp. 441–448.

[35] A. Satheesh, P. Muthukumar, and A. Dewan. "Computational study of metal hydride cooling system". In: *International journal of hydrogen energy* 34.7 (2009), pp. 3164–3172.

[36] A. F. Mills. *Basic heat and mass transfer*. Pearson, 2014, pp. 66–67.